Manuscript prepared for Atmos. Chem. Phys.
with version 3.2 of the LaTeX class copernicus.cls.
Date: 4 March 2011

A model study of the impact of source gas changes on the stratosphere for 1850-2100

E. L. Fleming[1,2], C. H. Jackman[1], R. S. Stolarski[1,3], and A. R. Douglass[1]

[1]NASA Goddard Space Flight Center, Greenbelt, Maryland
[2]Also at Science Systems and Applications, Inc., Lanham, Maryland
[3]Also at Department of Earth and Planetary Sciences, Johns Hopkins University, Baltimore, Maryland

Abstract. The long term stratospheric impacts due to emissions of CO_2, CH_4, N_2O, and ozone depleting substances (ODSs) are investigated using an updated version of the Goddard two-dimensional (2D) model. Perturbation simulations with the ODSs, CO_2, CH_4, and N_2O varied individually are performed to isolate the relative roles of these gases in driving stratospheric changes over the 1850-2100 time period. We also show comparisons with observations and the Goddard Earth Observing System chemistry-climate model simulations for the time period 1970-2100 to illustrate that the 2D model captures the basic processes responsible for long-term stratospheric change.

The 2D simulations indicate that prior to 1940, the ozone increases due to CO_2 and CH_4 loading outpace the ozone losses due to increasing N_2O and carbon tetrachloride (CCl_4) emissions, so that ozone reaches a broad maximum during the 1920s-1930s. This preceeds the significant ozone depletion during ~1960-2050 driven by the ODS loading. During the latter half of the 21^{st} century as ODS emissions diminish, CO_2, N_2O, and CH_4 loading will all have significant impacts on global total ozone based on the IPCC A1B (medium) scenario, with CO_2 having the largest individual effect. Sensitivity tests illustrate that due to the strong chemical interaction between methane and chlorine, the CH_4 impact on total ozone becomes significantly more positive with larger ODS loading. The model simulations also show that changes in stratospheric temperature, Brewer-Dobson circulation (BDC), and age of air during 1850-2100 are controlled mainly by the CO_2 and ODS loading. The simulated acceleration of the BDC causes the age of air to decrease by ~1 year from 1860-2100. The corresponding photochemical lifetimes of N_2O, $CFCl_3$, CF_2Cl_2, and CCl_4 decrease by 11-13% during 1960-2100 due to the acceleration of the BDC, with much smaller lifetime changes (<4%) caused by changes in the photochemical loss rates.

Correspondence to: E.L. Fleming (eric.l.fleming@nasa.gov)

1 Introduction

Changes in the atmospheric abundance of halogenated ozone depleting substances (ODSs) and the greenhouse gases (GHGs) CO_2, CH_4, and N_2O have been shown to significantly impact the chemical and dynamical structure of the stratosphere [e.g., World Meteorological Organization (WMO), 2007, 2011]. For example, much of the decline of stratospheric ozone during the 1980s and 1990s has been attributed to increased atmospheric halogen loading due to anthropogenic forcings. Increases in N_2O and the odd nitrogen species decrease ozone in the middle stratosphere [e.g., Crutzen, 1976], while increases in CO_2 and the subsequent cooling reduce the temperature dependent ozone loss rates and cause ozone increases in the upper stratosphere [e.g., Haigh and Pyle, 1979; Rosenfield et al., 2002].

Recent observational studies have detected the beginning of the ozone recovery process in the upper stratosphere, where ozone is most sensitive to changes in halogen loading [e.g., Reinsel, 2002; Newchurch et al., 2003]. However, detection of the change in the halogen influence on ozone can be complicated by the impacts due to long term changes in GHGs. It is therefore of interest to separate the relative impacts of the different chemical processes that control long term ozone changes.

Another important aspect of the changing atmospheric composition impact on the stratosphere is the quantification of photochemical lifetimes of the ODSs and GHGs. These lifetimes have come under recent scrutiny [Douglass et al., 2008], as they are important for deriving surface mixing ratio boundary conditions from emissions estimates for use in atmospheric models [Kaye et al., 1994; WMO, 2011]. The potential influence on lifetimes of the Brewer-Dobson circulation (BDC) acceleration due to climate change has also

been investigated [Butchart and Scaife, 2001; Douglass et al., 2008].

Most studies of past and future stratospheric change now utilize three-dimensional (3D) coupled chemistry-climate models (CCMs) [e.g., Eyring et al., 2006; Eyring et al., 2007; WMO, 2011]. Some 3D CCM investigations have shown the impact of different processes on long term stratospheric change, such as that due to the multi-decadal changes in ODS and GHG concentrations and sea surface temperatures (SSTs) [e.g., Butchart and Scaife, 2001; Austin et al., 2007; Olsen et al., 2007; Li et al., 2008; Eyring et al., 2010a; Eyring et al., 2010b; Austin et al., 2010]. However, performing numerous sensitivity simulations to separate the different chemical processes that control stratospheric changes can be more easily done using two-dimensional (2D) models, given their much smaller computational requirements. 2D models have been widely used in international assessments of the stratosphere [e.g., WMO, 2003, 2007, 2011], and past studies have shown that 2D models can resolve much of the large scale stratospheric variability on monthly and longer time scales, as seen in comparisons with observations and 3D models [e.g., Plumb and Mahlman, 1987; Yudin et al., 2000; Fleming et al., 2007; Newman et al., 2009]. Previous 2D model studies have investigated the relative roles of the long term changes in CO_2, CH_4, and N_2O, focussing on the stratospheric ozone changes over the next century [e.g., Randeniya et al., 2002; Chipperfield and Feng, 2003; Portmann and Solomon, 2007].

In this paper we expand on these previous studies and examine in more detail the relative contributions of the long term changes in atmospheric GHG and ODS loading using our recently upgraded Goddard Space Flight Center (GSFC) 2D coupled chemistry-radiation-dynamics model. We exploit the computational speed of the 2D model to perform numerous perturbation simulations to investigate the stratospheric impacts due to GHG and ODS loading for the 250-year time period, 1850-2100. We examine the ozone, temperature, and age of air impacts, and focus on the time periods prior to 1950 and the latter half of the 21^{st} century. We also use perturbation tests to examine the ozone impacts due to the chemical coupling between CH_4 and chlorine. We then investigate the long term time dependence of the photochemical lifetimes of N_2O, CFC-11, CFC-12, and CCl_4. Here, we examine the relative importance of changes in the BDC and the photochemical loss rates in controlling these lifetimes.

The recent SPARC Chemistry-Climate Model Validation Activity [SPARC CCMVal, 2010] provided a comprehensive process oriented evaluation of many CCMs. Because 2D models were not included in this activity, and given the recent improvements to our 2D model, we provide in Appendicies A and B, a detailed description and evaluation of our upgraded model, comparing climatological simulations with observations of various stratospheric tracers. Throughout the paper, we also compare long term simulations from the 2D model with the Goddard Earth Observing System chemistry-climate model (GEOSCCM) and multi-decadal observational data sets to illustrate that the 2D model captures the basic processes that drive long term changes in stratospheric ozone, temperature, and age of air. The good 2D model agreement with the measurements and the GEOSCCM then justifies the use of the 2D model for the perturbations addressed in this study.

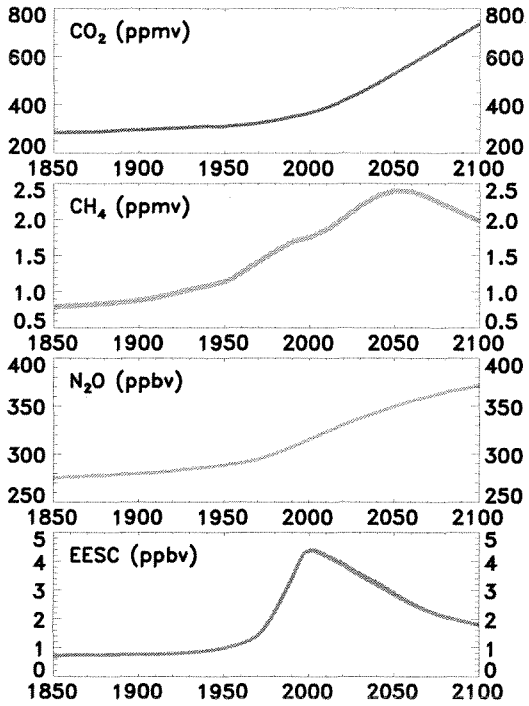

Fig. 1. Time dependent surface boundary conditions for CO_2, CH_4, and N_2O from Hansen and Sato [2004] for 1850-1950 and the IPCC GHG scenario A1B for 1950-2100. The bottom panel shows the upper stratospheric Equivalent Effective Stratospheric Chlorine (EESC) taken as the global average of $Cl_y + 60Br_y$ at 50 km. See text for details.

2 Model Simulations

For this study, we utilize a series of 2D model experiments in which the surface concentrations of only the ODSs or the individual GHGs are varied time dependently for 1850-2100, while all other source gases are fixed at low (1850) levels. In this way, we separate the individual effects of the ODS and GHG loading. We compare these with the 2D baseline simulation in which all source gases are varied time de-

pendently, and with the GEOSCCM baseline simulation for 1950-2100. The GEOSCCM couples the GEOS-4 general circulation model with stratospheric chemistry and has been applied to various stratospheric problems [e.g., Stolarski et al., 2006; Pawson et al., 2008; Waugh et al., 2009; Oman et al., 2009; Newman et al., 2009; Li et al., 2009]. The GEOSCCM uses specified time dependent SSTs and sea-ice amounts, and the results presented in this study are comprised of three simulations which utilize somewhat different SSTs for the past and future time periods: 1950-2004, 1971-2052, and 1996-2100.

For 1950-2100, the 2D and GEOSCCM simulations use surface ODS boundary conditions from scenario A1 of WMO [2007], and GHG boundary conditions from scenario A1B (medium) from the Intergovernmental Panel on Climate Change (IPCC) Special Report on Emissions Scenarios [IPCC, 2000]. The 2D simulations for 1850-1950 use GHG surface boundary conditions from Hansen and Sato [2004]. For the ODSs, most are zero prior to 1950, except for the following: $CFCl_3$ and CF_2Cl_2 are set to zero prior to 1935 and 1946, respectively, and are then ramped up slowly to the 1950 WMO [2007] values. CCl_4 is ramped up exponentially from zero in 1900 to the 1950 value of WMO [2007], approximating the time series of Butler et al. [1999]. CH_3Cl and CH_3Br are set to 440 pptv and 5 pptv respectively in 1850, and follow the time variation up to 1950 as discussed in Butler et al. [1999] and WMO [2003]. The corresponding GHG surface boundary conditions for 1850-2100 are shown in Figure 1, along with the Equivalent Effective Stratospheric Chlorine (EESC, bottom panel) representing the time dependent concentration of halogen loading from the ODS source gases. Here, EESC is taken as the global average of $Cl_y + 60Br_y$ at 50 km. Note that all 2D and GEOSCCM calculations use fixed solar flux (no solar cycle variations) and clean stratospheric aerosol conditions specified from WMO [2007].

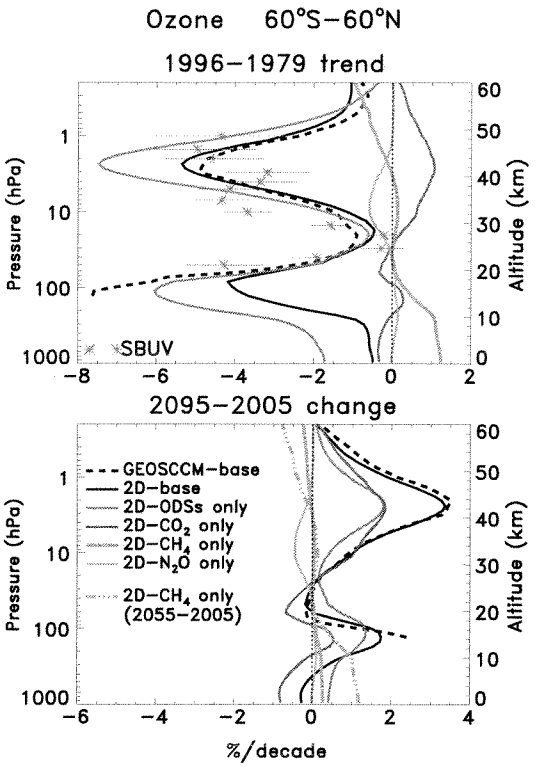

Fig. 2. (Top) Vertical profiles of the annual and near-global average (60°S-60°N) ozone trend (%/decade) for 1996-1979 derived from the SBUV data and model simulations. Shown are the base simulations (all source gases varied time dependently) of the GEOSCCM (black dashed lines) and 2D model (black solid lines), along with 2D simulations in which only certain source gases are varied as follows: ODSs only (blue lines); CO_2 only (red lines); CH_4 only (orange lines); N_2O only (green lines). The trends are derived from regression fits to the EESC time series (Figure 1) for 1979-2004. (Bottom) As in the top but for the 2095-2005 ozone difference (%/decade) using 10-year averages centered on 2095 and 2005 to reduce the effects of interannual dynamical variability in the GEOSCCM. The change due to CH_4 is shown for 2095-2005 (orange solid) and 2055-2005 (orange dashed-dotted).

3 Ozone

3.1 Base model-data comparisons

As a general model evaluation, we first compare the simulated vertical profile ozone trends for 1979-1996 with the SBUV data for the near-global (60°S-60°N) average (Figure 2, top). These are derived from regression fits to the EESC time series (Figure 1) for 1979-2004. At 50 hPa (the lowest level of the SBUV data), the observationally-derived trend is underestimated in the 2D base simulation (all source gases varied time dependently), less so in the GEOSCCM. However above 20 km, both base simulations are mostly in reasonable agreement with the observations. Note that we do not show GEOSCCM results in the troposphere as ozone is relaxed to an observational climatology in this region.

The recent past and future ozone changes in the 2D model are also mostly similar to the GEOSCCM in the near global average (Figure 2) and in the latitude-height variations (Figures 3 and 4). This general model agreement is also seen in time series of near-global profile ozone (Figure 5), global total ozone (Figure 6), and tropical total ozone (Figure 7). For reference, we include time series of the BUV/SBUV satellite observations for profile ozone and ground-base data for global total ozone (updated from Fioletov et al. [2002]).

The largest 2D-GEOSCCM differences occur in the Antarctic ozone hole region, where the 2D model simulates smaller past (negative) and future (positive) ozone changes

compared to the GEOSCCM (Figures 3 and 4). Some of this is likely due to the 2D model not fully resolving the processes that control polar ozone loss, as these can have large zonal asymmetries. Some of this model difference also reflects the known high ozone bias in the high latitude lower stratosphere in the GEOSCCM. This bias is most pronounced during periods of low chlorine loading so that the chlorine-induced changes in the Antarctic spring are too large by 60-80% [Pawson et al., 2008]. These model differences are reflected in the near-global averaged vertical profiles below 18 km (Figure 2) and in the total column time series (Figure 6) in which the GEOSCCM simulates significantly more past ozone reduction and future ozone increase. However, the generally good agreement between the 2D model base simulations and the observations and GEOSCCM in Figures 2-7 show that the 2D model captures the basic processes responsible for long term stratospheric ozone changes.

3.2 2D perturbation simulations

The relative roles of ODS, CO_2, CH_4, and N_2O loading in controlling the recent past and future ozone changes are illustrated by the 2D model perturbation simulations in Figures 2-7. This includes the well known dominance of ODS loading in controlling the sharp ozone decline in the lower and upper stratosphere globally during ~1970-2000. Because of the strong impact in the upper stratosphere (Figures 3 and 4), ODS loading also largely controls the tropical total ozone time series from ~1970 through the early 21^{st} century (Figure 7).

CO_2 cooling and subsequent reduction in the ozone loss rates produce a broad ozone increase of 1-2%/decade in the upper stratosphere (Figures 2-4). For the 2005-2095 time period, the ozone increases due to increasing CO_2 and declining ODS emissions are similar in the upper stratosphere (1.5-2%/decade) in Figure 2 (bottom) and Figure 4. By 2100, CO_2 loading is the dominant impact at 40 km, causing a 20% increase in ozone from 1850-2100 (Figure 5, middle, red curve).

Previous CCM studies have shown that increased GHG loading results in an acceleration of the BDC with related impacts on ozone and trace gases [e.g., Butchart and Scaife, 2001; Austin and Li, 2006; Garcia and Randel, 2008; Li et al., 2009]. This feature is seen in the 2D CO_2-only simulation in Figures 3 and 4, in which lower tropical stratospheric ozone is reduced by 1-2%/decade as ozone-poor air is advected upwards from the tropical troposphere. There is a compensating downward advection of ozone-rich air in the extratropics at 10-15 km which is strongest in the NH. This hemispheric asymmetry is consistent with previous GEOSCCM simulations of the climate change impacts on ozone [Olsen et al., 2007; Li et al., 2009; Waugh et al., 2009]. These BDC-driven ozone changes are reflected in the global average in Figure 2, with an ozone decrease (increase) of ~ 0.5%/decade centered near 20 km (15 km) in the 2D

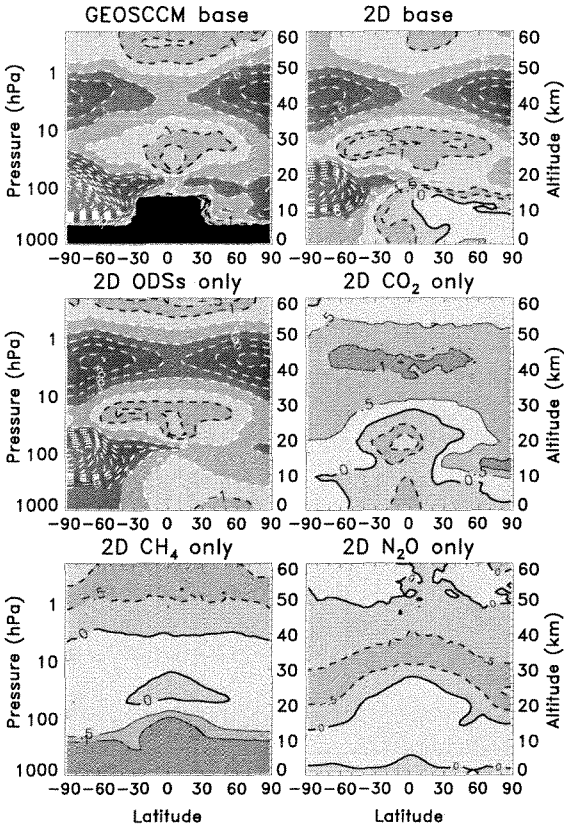

Fig. 3. Annually averaged ozone trend for 1996-1979 derived from the GEOSCCM and 2D model simulations. The top panels are from the base simulations in which all source gases are varied time dependently. The middle and bottom panels show 2D simulations in which only the ODSs or GHGs are varied time dependently as indicated. The trends are derived from regression fits to the EESC time series (Figure 1) for 1979-2004. The GEOSCCM trends are not computed in the troposphere as ozone is relaxed to a climatology in this region. The contour intervals are ±2 %/decade and include the ±.5 and ±1 %/decade contours.

CO_2-only simulation. The CO_2-induced ozone decrease is dominant by 2100 in the near global average time series at 22 km (Figure 5, bottom, red curve), with a decrease of 5.5% from 1850-2100. At this level, N_2O and CH_4 loading have negligible impacts, so that the net result of ODS and CO_2 changes is an ozone increase from 2000-2030 and a decrease from 2030-2100 in the base simulations.

The net impact of CO_2 loading on total ozone is an increase of 12.5 DU (4.2%) from 1850-2100 in the global average (Figure 6, red curve). CO_2 loading also increases total ozone at midlatitudes of both hemispheres (not shown), and as with profile ozone, the total column increase is more pronounced in the NH compared to the SH midlatitudes owing to the larger enhancement of the BDC north of the equator.

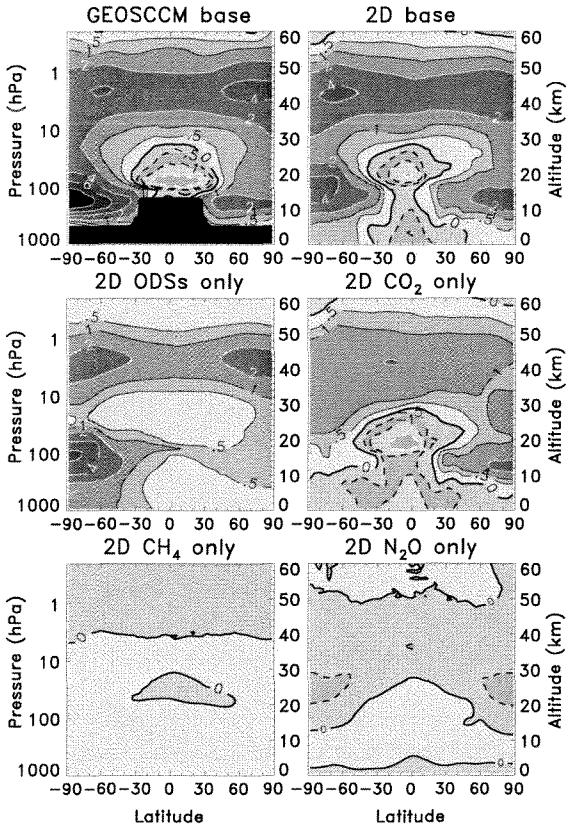

Fig. 4. As in Figure 3, except for the 2095-2005 ozone difference using 10-year averages centered on 2095 and 2005 to reduce the effects of interannual dynamical variability in the GEOSCCM. The contour intervals are ±2 %/decade and include the ±.5 and ±1 %/decade contours.

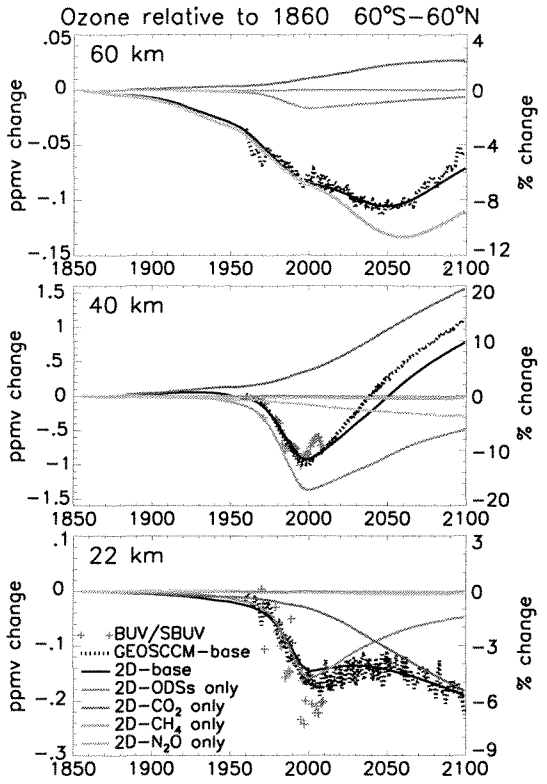

Fig. 5. Near global (60°S-60°N) annually averaged ozone time series for 1860-2100, relative to 1860, at 22, 40, and 60 km. Values are in ppmv change (left axes) and % change (right axes). Shown are the base simulations (all source gases varied time dependently) of the GEOSCCM (black dotted lines) and 2D model (black solid lines), along with 2D simulations in which only certain source gases are varied as indicated. The GEOSCCM time series has been adjusted to match the 2D base simulation for 1960. Also shown are the BUV/SBUV satellite observations for 1970-2009 (excluding 1973-1978) at 22 and 40 km ("+" symbols). To emphasize the model-data comparison after 1970, the data have been adjusted so that the 1970-1972 average matches that of the base simulations.

In the tropics, the enhancement of the BDC advecting ozone-poor air from the troposphere counteracts the ozone increase in the upper stratosphere caused by the CO_2 cooling. The net effect is a decrease in tropical total column ozone throughout the 21^{st} century in Figure 7 (red curve), consistent with previous CCM results [Li et al., 2009; Waugh et al., 2009; Eyring et al., 2010b].

In Figures 2-5, N_2O loading and the subsequent increase in stratospheric NO_y lead to a decrease in stratospheric ozone, with a maximum decline of −0.5 to −0.6%/decade near 35 km in the global average in both the past and future. These magnitudes are slightly less than obtained by Portmann and Solomon [2007] who used the IPCC A2 GHG scenario which has larger N_2O increases compared to the A1B scenario used here. From 1850-2100, N_2O loading results in a total ozone decrease of 8 DU (−2.7%) in the global average (Figure 6) and 4 DU (−1.5%) in the tropics (Figure 7). This effect of N_2O loading taken in isolation is larger than would be when taking into account the effects of increased CO_2 cooling on future NO_y and ozone changes, as has been discussed previously [Rosenfield and Douglass, 1998; Daniel et al., 2010]. We will discuss this in more detail in section 3.5.

Atmospheric CH_4 impacts ozone via three mechanisms: 1) increases in CH_4 increase the amount of H_2O in the stratosphere and mesosphere which in turn reduces ozone by enhancing the HO_x-ozone loss cycles; 2) increases in CH_4 lead to increased ozone throughout the stratosphere by converting active chlorine to the reservoir HCl via the reaction $CH_4 + Cl \rightarrow HCl + CH_3$; and 3) increases in CH_4 lead to increased ozone in the troposphere and very lower stratosphere due NO_x-induced ozone production [e.g, Brasseur

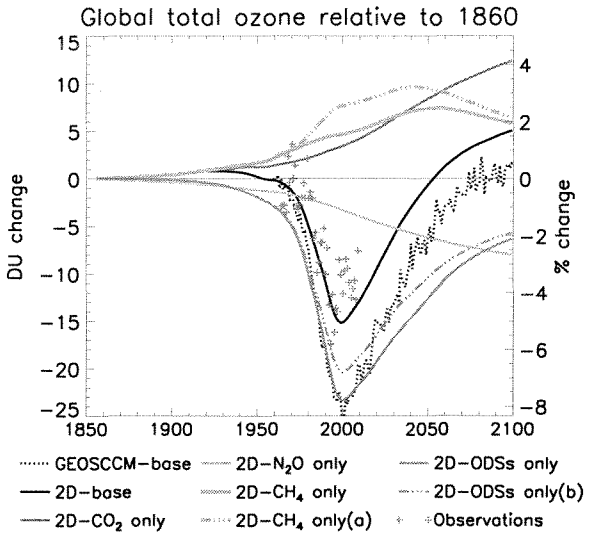

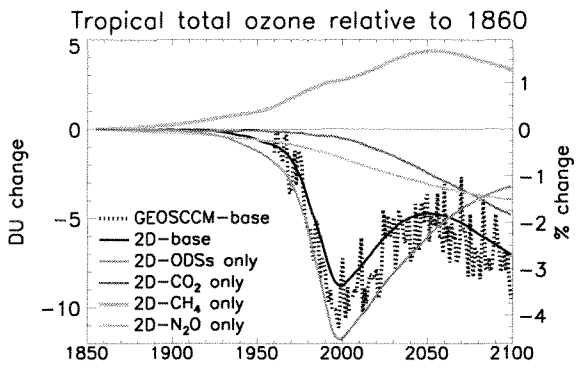

Fig. 6. Global and annual averaged total ozone time series relative to 1860 values. Shown are the base simulation (all source gases varied time dependently) from the 2D model (black solid line) and GEOSCCM (black dotted line). The GEOSCCM time series has been adjusted to match the 2D base simulation for 1960. Also shown are 2D simulations in which only certain source gases are varied time dependently as indicated, with the other source gases fixed at 1850 levels. The "+" symbols represent ground-based data updated from Fioletov et al. [2002]. To emphasize the model-data comparison after 1970, the data have been adjusted so that the 1964-1970 average matches that of the base simulations. Also shown are the combined effects of CH_4 and ODSs loading: the 2D-CH_4 only(a) curve (orange dashed-dotted) is the difference between a simulation with CH_4 and the ODSs varied time dependently and that with only the ODSs varied time dependently, showing the effect of CH_4 in the presence of time dependent ODS loading; the 2D-ODSs only(b) curve (blue dashed-dotted) is the difference between a simulation with CH_4 and the ODSs varied time dependently and that with only CH_4 varied time dependently, showing the effect of ODSs in the presence of time dependent CH_4 (CO_2 and N_2O are fixed at 1850 levels in these simulations). Values are in Dobson Unit (DU) change (left axes) and % change (right axes).

Fig. 7. As in Figure 6 except for tropical total ozone (10°S-10°N average), and without the 2D-CH_4 only(a) and 2D-ODSs only(b) curves. For visual clarity, the observations are not shown as these are dominated by the large quasi-biennial oscillation, a feature not included in the simulations. Values are in Dobson Unit (DU) change (left axes) and % change (right axes).

and Solomon, 1986]. This latter mechanism is strongly dependent on the amount of tropospheric NO_x. To more properly account for this in the 2D model, we constrain the model troposphere using output from the Global Modeling Initiative's (GMI) combined stratosphere-troposphere chemistry and transport model (GMI Combo CTM) [Strahan et al., 2007; Duncan et al., 2007]. This includes specifying the lower tropospheric (below 5 km) NO_y boundary condition to account for surface emission and loss processes, NO_x production from lightning, and washout of HNO_3, all for present day conditions. The resulting 2D tropospheric NO_x and NO_y distributions compare favorably with the GMI model. The 2D model utilized in this way simulates a mid-upper tropospheric ozone response to a steady state CH_4 perturbation (0.5 ppmv) similar to that obtained in the GMI model for present day conditions.

Figures 2-5 show that the combined effect of the three CH_4 mechanisms outlined above yield a significant ozone increase (1-1.5 %/decade) in the troposphere and very lower stratosphere, a mostly weak positive response at 20-40 km, and a negative ozone response above 40 km with decreases

of -1%/decade and larger above 60 km. Figure 5 (top panel) shows that CH_4 loading is dominant in controlling the ozone time dependence at 60 km, due to the subsequent increase in H_2O and HO_x-ozone loss. This mechanism also results in significant CH_4-induced ozone loss at 60 km prior to 1960 so that one-third of the total decrease in ozone during 1850-2050 has occurred by 1960. For total ozone, CH_4 loading results in increases from 1850-2050 of 7.5DU (2.5%) in the global average (Figure 6) and 4.5 DU (1.7%) in the tropics (Figure 7).

The future ozone response to CH_4 follows the surface boundary condition, which is significantly larger in 2055 than in 2100 in the A1B scenario (Figure 1). This results in a relatively small change from 2005-2095 seen in the latitude-height section in Figure 4 ($< \pm 0.5\%$/decade everywhere). We show vertical profile results for both 2005-2055 and 2005-2095 in Figure 2, illustrating the much different magnitudes of the response for the different time periods. These responses are also qualitatively similar but have smaller magnitudes compared to Portmann and Solomon [2007] who used IPCC scenario A2 which has larger GHG loading. We note that because the 2D model tropospheric NO_x and NO_y are fixed to the present day GMI simulation, the tropospheric ozone response to the time dependent CH_4 perturbation shown in Figures 2-7 does not account for long term changes in tropospheric NO_x emissions. These have undergone significant past increases which would lead to more CH_4-induced tropospheric ozone production than we show in Figures 2-7.

By 2100, ODS, CO_2, CH_4, and N_2O loading all play important roles in controlling global total ozone. CO_2 has the largest impact, leading to a 4% increase from 1860-2100, with CH_4 loading causing a 2% increase, and N_2O and ODS loading each contributing a 2-2.5% decrease from 1860-2100 (Figure 6). The net result is a 1.7% (5DU) increase from 1860-2100 in the 2D base simulation. In the tropics, baseline total ozone increases during 2000-2050. This is followed by a $\sim 1\%$ decrease over the second half of the century, as the combination of increasing CO_2 and N_2O and decreasing CH_4 more than offset the effect of reduced ODS loading. This general time variation of 21^{st} century tropical total ozone is consistent with the GEOSCCM in Figure 7 and other CCM results reported recently [Eyring et al., 2010a, 2010b; Austin et al., 2010].

3.3 1860-1960 Ozone

As seen in Figures 5-7, the ozone changes prior to 1960 are relatively small, but not insignificant, compared to post-1960. To examine this more closely, Figure 8 shows a close-up of the 1860-1960 ozone time series for the near-global average at 40 km and the global average total column.

From 1860-1960, the total column impacts due to CO_2 and N_2O are approximately equal and opposite, being $+0.5\%$ and -0.5%, respectively. The CH_4 impact is slightly larger by 1960 ($+0.75\%$). The ODS impact, which is due mainly to CCl_4 emissions, causes a 1% depletion in the total column by 1960, with the vast majority of this decrease occuring after 1920. At 40 km, the impact of CO_2 cooling leads to a 2% ozone increase from 1860-1960, which is approximately equal and opposite to the ozone depletion caused by ODSs.

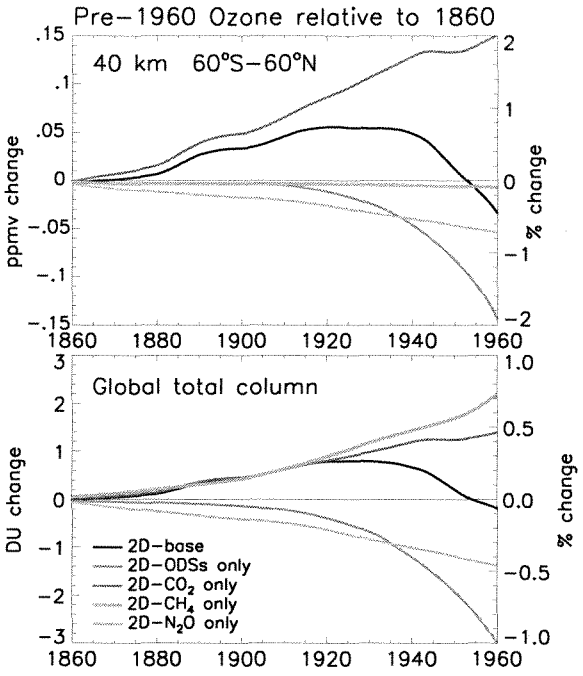

Fig. 8. Ozone time series for 1860-1960, relative to 1860 values, from 2D model simulations for the 60°S-60°N average at 40 km (top), and the 90°S-90°N average total column (bottom). Shown are the base simulation (all source gases varied time dependently) and simulations in which only certain source gases are varied time dependently as indicated, with the other source gases fixed at 1860 levels. Values are in Dobson Unit (DU) change (left axes) and % change (right axes).

Ozone in the resulting base simulation (black curves) reaches broad pre-modern maxima during 1920-1940, with increases from 1860 of 0.8 DU (0.3%) in the total column and 0.06 ppmv (0.8%) at 40 km. This preceeds the decline in ozone driven mainly by ODS loading, which becomes much more rapid after $\sim$1970 (Figures 5 and 6).

3.4 CH_4 sensitivity experiments

As the changes in CH_4 impact ozone via the different mechanisms outlined above, we now examine these effects in more detail. Figure 9 (top panel) shows the global/annual averaged 2D model steady state ozone change due to a 0.5 ppmv CH_4 perturbation for year 2000 conditions. This is expressed in DU/km to emphasize the contribution to the total column change. CH_4 is lost via reaction with $O(^1D)$, OH, and Cl, and the black curve shows the standard case in which all three reactions use the perturbed CH_4. This shows that the CH_4 impact on ozone is positive everywhere below 46 km, with only a very small negative change above 46 km, and a total column response of +2.7DU.

To qualitatively separate the effects of the different mechanisms, the green curve is a simulation in which perturbed CH_4 is used for the reactions with $O(^1D)$ and OH, with unperturbed CH_4 used for the reaction $CH_4 + Cl$. In this way, the conversion of active chlorine (Cl) to the reservoir (HCl) is not impacted by the additional CH_4. Therefore, ozone only responds to the enhanced NO_x-induced ozone production in the troposphere yielding ozone increases in this region, and the enhanced H_2O and HO_x-ozone loss cycles above ~35 km and in the very lower stratosphere, which yield ozone decreases. The enhanced H_2O in this case also enhances polar stratospheric clouds and the heterogeneous chemical ozone loss in the SH polar region, which results in a negative response at 17-28 km in the global average in Figure 9.

The red curve in Figure 9 shows the opposite case of the green curve, i.e., here, perturbed CH_4 is used for the reaction $CH_4 + Cl$, with unperturbed CH_4 used for the reactions with $O(^1D)$ and OH. This significantly reduces the amount of H_2O and HO_x-ozone loss, as well as the NO_x-ozone production in the troposphere generated by the CH_4 perturbation. This better isolates the impact of CH_4 in controlling the chlorine partitioning and subsequent chlorine-catalyzed ozone loss. The resulting ozone response is positive throughout the stratosphere, with the largest impacts occurring in the regions where chlorine-catalyzed ozone destruction is largest, i.e., the upper stratosphere globally, and in the lower stratosphere corresponding to the ozone hole region. Comparing the green and red curves shows that the $CH_4 + Cl$ reaction has the largest impact on ozone at ~15-45 km, with the NO_x-ozone production mechanism being dominant below 15 km.

The bottom panel in Figure 9 shows the same cases run for 2100 conditions, which has greatly reduced chlorine loading compared with present day conditions. The effect of the future reduced chlorine loading is evident, as the case in which the perturbed CH_4 is used only for the $CH_4 + Cl$ reaction (red curve) exhibits a much weaker ozone response at all levels compared with the simulations for present day conditions. For the total column, this simulation accounts for only 28% of the full CH_4 response (+1.8DU) in 2100, compared to 70% of the full response in 2000. In 2100, the full ozone response to the CH_4 perturbation (black curve) is dominated below ~18 km by the enhanced NO_x-ozone production, and above ~45 km by the enhanced HO_x-ozone loss.

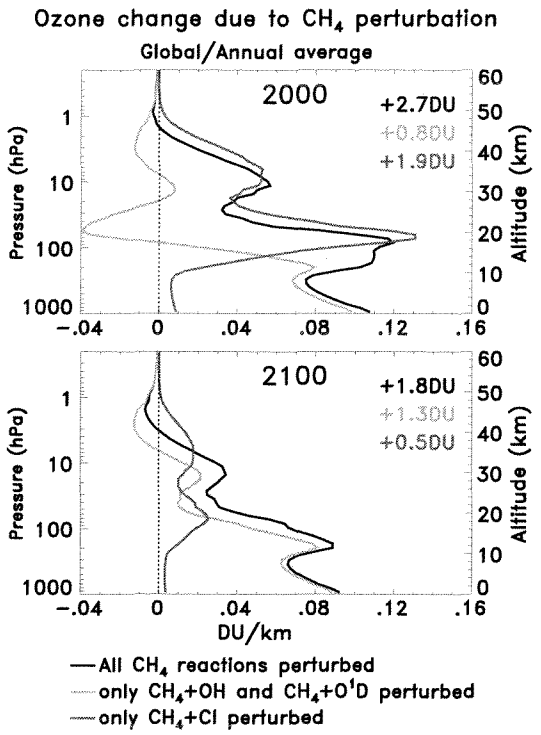

Fig. 9. Vertical profiles of the annual and global averaged steady state ozone change (DU/km) due to a 0.5 ppmv CH_4 perturbation for year 2000 (top) and year 2100 (bottom). The black curves show simulations with all CH_4 reactions (reactions with $O(^1D)$, OH, and Cl) using perturbed CH_4. The green curves show simulations using perturbed CH_4 for reactions with $O(^1D)$ and OH, with unperturbed CH_4 used for the reaction $CH_4 + Cl$. The red curves show simulations using perturbed CH_4 for the reaction $CH_4 + Cl$ with unperturbed CH_4 used for reactions with $O(^1D)$ and OH. The total column responses for each case are listed in the upper right corner of each panel.

For time dependent total ozone, the combined effect of CH_4 and Cl_y loading is illustrated in Figure 6. The solid orange curve (2D-CH_4 only) uses fixed 1850 (very low) chlorine loading, and is therefore similar to the green curves in Figure 9 (unperturbed $CH_4 + Cl$) since the impact of the $CH_4 + Cl$ reaction is minimal in this case. To illustrate the full effect of CH_4 in the presence of time dependent ODS loading (analogous to the black curves in Figure 9), the 2D-CH_4 only (a) curve (orange dashed-dotted in Figure 6) is the difference between a simulation with CH_4 and the ODSs var-

ied time dependently and that with only the ODSs varied time dependently (CO_2 and N_2O are fixed at 1850 levels in both simulations). Compared to the simulation using fixed 1850 Cl_y (solid orange line), the full effect of CH_4 loading results in significantly more global total ozone when the ODS loading is highest, i.e., ~1985 through the first half of the 21^{st} century.

This effect can also be seen in the ODS-only simulation, i.e., the effect of ODS loading in the presence of time dependent CH_4 (the 2D-ODS only (b) curve (blue dashed-dotted) in Figure 6). This is the difference between the simulation with CH_4 and the ODSs varied time dependently and that with only CH_4 varied time dependently. Comparing the two blue curves illustrates how the impact of the ODS loading is mitigated by the time dependent CH_4 changes. This effect is largest when the ODS loading is largest, i.e., ~2000, when the global total ozone depletion due to ODS loading is 3 DU (1%) less in the presence of the time dependent CH_4 changes compared to that with fixed 1850 CH_4 levels.

3.5 Quantification of the Ozone Impacts due to GHGs

Given the importance of increasing GHG emissions on future ozone levels, we examine these relative impacts in more quantitative detail. To do this, we apply the concept of the Ozone Depletion Potential (ODP) to GHG emissions, as recently done for N_2O and the induced NO_x-ozone destruction [Ravishankara et al., 2009; Daniel et al., 2010]. Traditionally, the ODP metric has been used to quantify the change in global ozone per unit mass emission of a specific chlorine-containing compound relative to the change in global ozone per unit mass emission of CFC-11 ($CFCl_3$) [Wuebbles, 1983; Fisher et al., 1990; Solomon et al., 1992]. Because the ODP is defined as a ratio to the ozone loss due to CFC-11, many uncertainties in the ozone-loss computation cancel. For this reason ODPs of chlorocarbon compounds are generally less sensitive to photochemical modelling uncertainties than are absolute ozone loss calculations.

Application of the ODP concept to a non-chlorine containing compound does not benefit in the same way from the cancellation of uncertainties in the ratio of ozone loss to that of CFC-11, e.g. N_2O does not cause an ozone hole. More generally, the chemical mechanisms that impact ozone are different for GHGs, and tend to occur in different regions of the atmosphere, compared to those of chlorine containing compounds.

While being cautious about the interpretation of the ODP concept as applied to non-chlorine containing compounds, we use the ODP metric to examine the relative impacts on ozone of N_2O, CH_4, CO_2, and CFC-11 for 1850, 1950, 2000, and 2100 steady-state atmospheric conditions. These calculations are meant as a guide for evaluating the relative importance of GHG loading on past and future ozone levels.

We use the standard method to calculate ODPs, i.e., change each species by an amount that leads to a 1% change in annually-averaged global total ozone. Table 1 shows the resulting annual and global average flux of each compound for the years indicated. The ozone change is negative for CFC-11 and N_2O, and positive for CH_4 and CO_2. Note that the flux changes for N_2O, CH_4 and CO_2 are much larger, by one to three orders of magnitude, than those for CFC-11. Table 2 shows these numbers converted to the standard ODP, i.e., the ratio of the flux change needed to cause a 1% ozone change for each compound to the flux change for CFC-11. Our N_2O ODP values for 1950 and 2000 (+0.024 and +0.019, respectively), are similar to those reported in Ravishankara et al. [2009]. These results also illustrate that while N_2O has a positive ODP, CH_4 and CO_2 have negative ODPs relative to CFC-11. However because the fluxes and ODPs vary by two orders of magnitude, and the background concentrations also undergo large changes, it is difficult to evaluate these values on an absolute basis or relative to one another.

Tables 3 and 4 illustrate another way to look at the problem of comparing the impact of GHGs on ozone. Table 3 shows the sensitivity of total column ozone to a specified change in the concentration of each GHG. These are expressed in percent change in ozone for a 1 ppbv or 1 ppmv change in the surface concentration of the GHGs. The impact of each can then be deduced by multiplying by the actual change in the concentration of the species over a given time period. This is

Table 1. Steady state 2D model calculated annual/global average flux (kg/sec) required to produce a 1% change in annually averaged global total ozone for the compounds and years listed. The ozone change is negative for CFC-11 and N_2O, and positive for CH_4 and CO_2.

	1850	1950	2000	2100
CFC−11	1.52	1.65	2.02	1.83
N_2O	61.9	68.5	107	104
CH_4	4980	4960	3130	5960
CO_2	241	269	519	881

Table 2. Steady state 2D model calculated ozone depletion potential (ODP) relative to CFC-11 for N_2O,CH_4, and CO_2 for the years indicated, based on the values listed in Table 1.

	1850	1950	2000	2100
N_2O	+0.025	+0.024	+0.019	+0.018
CH_4	−0.00031	−0.00033	−0.00065	−0.00031
CO_2	−0.0063	−0.0062	−0.0039	−0.0021

Table 3. Steady state 2D model calculated percentage change in annual/global average total ozone per unit mixing ratio change for the compounds and years listed. The mixing ratios are in parts per billion by volume (ppbv) for N_2O, and parts per million by volume (ppmv) for CH_4 and CO_2. Shown in parentheses are the percentage changes of each compound, relative to the background levels, required to produce a 1% ozone change.

	1850	1950	2000	2100
N_2O	−0.031 (12)	−0.028 (13)	−0.020 (16)	−0.021 (13)
CH_4	+1.8 (70)	+1.7 (49)	+2.6 (22)	+1.4 (36)
CO_2	+0.016 (23)	+0.014 (23)	+0.0077 (34)	+0.0041 (33)

Table 4. Percentage change in annual/global average total ozone for the compounds and time intervals listed, based on the sensitivity factors in Table 3 and the change in the surface boundary condition in the A1B scenario (Figure 1). The CH_4-induced ozone change is negative for 2080-2100 due to the decrease in the methane boundary condition during this time.

	1940-1960	1980-2000	2080-2100
N_2O	−0.12	−0.30	−0.15
CH_4	+0.31	+0.49	−0.30
CO_2	+0.07	+0.25	+0.34

similar to the method used in Stolarski et al. [2010] for temperature changes. The resulting percentage ozone changes for several 20-year periods are listed in Table 4. Note that the CH_4-induced ozone change is negative for 2080-2100 since the methane boundary condition decreases during this time period (Figure 1). These calculations illustrate that CH_4 had the largest GHG impact on ozone during 1980-2000, owing to the large effect of high Cl_y loading, with the N_2O and CO_2 impacts being roughly equal and opposite. The CH_4 impact was also substantially larger than either N_2O or CO_2 during 1940-1960, reflecting the large relative changes in the CH_4 boundary condition during this time. However at the end of the 21^{st} century, the CO_2 impact is projected to be the largest, and will be more than twice the magnitude of the N_2O impact.

Table 3 also shows the sensitivities as percent changes to the background levels of each GHG, required to produce a 1% ozone change (listed in parentheses). For N_2O, a ~15% change in the background is required to cause a 1% change in ozone, compared to a ~25-35% change for CO_2, and ~20-70% change for CH_4.

The time dependence of the values in Tables 1-3 partly reflects the fact that as the background concentrations increase, more flux of a substance is required to produce a 1% ozone change. However, this time dependence also reveals interesting aspects of the interactions of the perturbations. For CFC-11, increasing levels of N_2O (NO_y) and CH_4 convert active chlorine to the reservoirs $ClONO_2$ and HCl, respectively, thereby reducing the efficiency of ClO_x-ozone destruction.

For N_2O, the time dependence is partly due to the changing background Cl_y, i.e., with higher Cl_y more NO_x is tied up in $ClONO_2$, thereby reducing the efficiency of the NO_x-ozone loss. Other factors include: 1) the CO_2 cooling of the stratosphere which results in greater chemical destruction of NO_y [Rosenfield and Douglass, 1998], and therefore reduced $NO_x - O_3$ loss; and 2) a general decrease in $O(^1D)$, by as much as 10%, from ~1970-2100 throughout most of the stratosphere which results in less NO_x production via the reaction $N_2O+O(^1D)$. As a result of these factors, our N_2O ODP in 2100 is a bit smaller than in 2000. The N_2O ODPs for 1850 and 1950 are very similar, as are the CH_4 and CO_2 ODPs, reflecting the small GHG and EESC-induced changes in the stratosphere prior to 1950 (Figures 5 and 6).

The ozone impact of CH_4 is strongly dependent on the atmospheric chlorine loading, via the reaction $CH_4 + Cl$ which affects the partitioning of Cl_y (e.g., Figures 6 and 9). As a result, significantly less CH_4 flux is required (Table 1) to get a 1% ozone increase in 2000 (large Cl_y loading) compared to 1850, 1950, and 2100 (small Cl_y loading). Similarly, the CH_4 perturbation as a percentage of the background (Table 3) is significantly smaller in 2000 compared to the other years. The resulting CH_4 ODP is nearly twice the magnitude in 2000 compared to 1950, 1950, or 2100. As discussed earlier, the CH_4 results presented here do not account for changes in tropospheric NO_x emissions (the model uses fixed present day NO_y specified from the GMI simulations). These likely undergo significant past and future changes [IPCC, 2007], with less (more) NO_x leading to less (more) tropospheric ozone production and a smaller (larger) negative CH_4 ODP than we report in Table 2.

For CO_2, the strong time dependence in Tables 1-3 is mostly due to the changing background concentration, which increases by a factor of 2.5 from 1850-2100 (Figure 1). However, the percentage change relative to the background in Table 3 is somewhat larger in 2000 and 2100 than in 1850 and 1950. This is partly due to the fact that CO_2 cooling and the corresponding increase in upper stratospheric ozone become less efficient at higher CO_2 levels, i.e., a saturation effect [e.g., Ramaswamy et al., 2001a]. There are other higher order effects that influence this CO_2 time dependence, including the future changing PSC concentrations - due to stratospheric cooling and increasing water vapor - coupled with the decreasing halogen loading.

4 Temperature

Previous studies have investigated stratospheric temperature trends in the recent past and future, including the relative

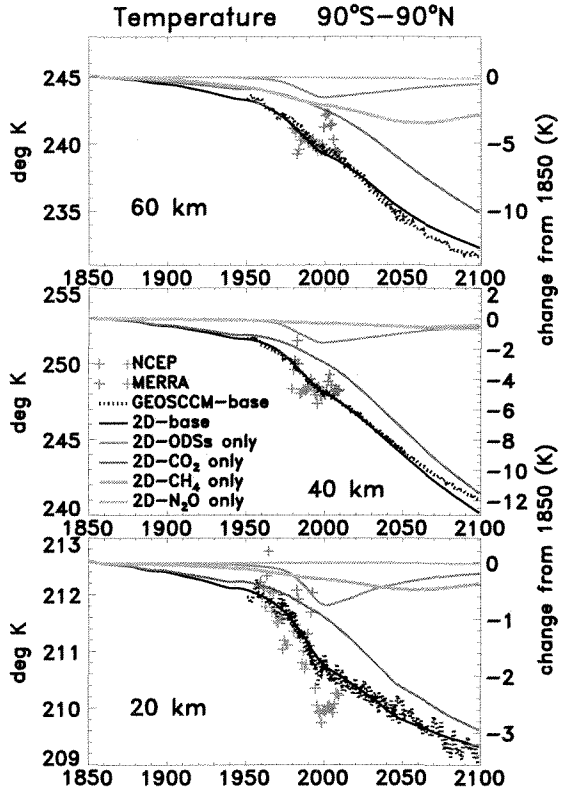

Fig. 10. Global and annually averaged temperature time series for 1850-2100 at 20, 40, and 60 km from the base simulations (all source gases varied time dependently) of the GEOSCCM (black dotted lines) and 2D model (black solid lines). Also shown are 2D simulations in which only certain source gases are varied time dependently as indicated. The right hand axes show the changes relative to 1850. The observations are from the NCEP reanalysis and reanalysis-2 data at 20 km for 1958-2009 (blue "+"), and the new NASA Modern Era Retrospective-analysis for Research and Applications (MERRA) meteorological analyses for 1979-2009 at 40 and 60 km (purple "+"). To account for the systematic differences between the models and data, we have added the following offsets to the models at 20, 40, and 60 km, respectively: 2D model: 0K, −3.4K, −1.5K; GEOSCCM: −2.7K, +1.3K, −2K.

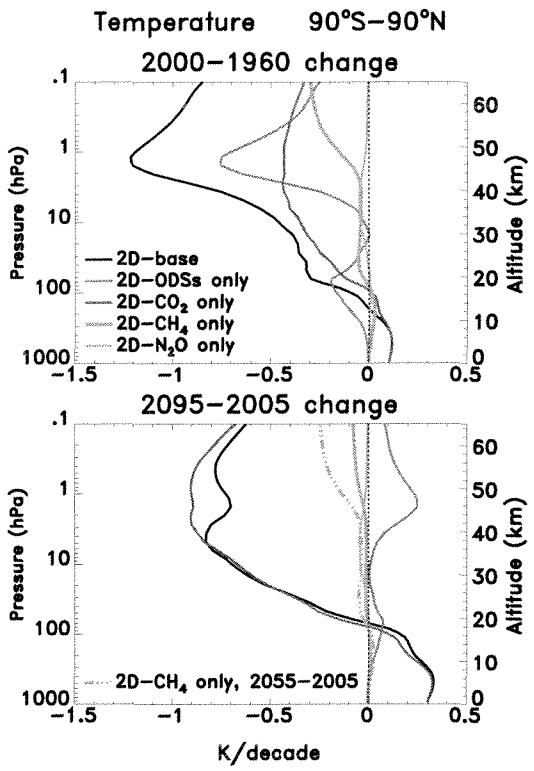

Fig. 11. (Top) Vertical profiles of the annual and global averaged temperature change (K/decade) for 2000-1960 (top) and 2095-2005 (bottom) from the 2D model simulations as indicated. The change due to CH_4 is shown for 2095-2005 (orange solid) and 2055-2005 (orange dashed-dotted) in the bottom panel.

contributions of ODS and GHG loading [e.g., Ramaswamy et al., 2001b; Shine et al., 2003; Shepherd and Jonsson, 2008; Stolarski et al., 2010]. Here we briefly summarize the model simulated temperature changes, focussing on the relative contributions of CO_2, CH_4, and N_2O.

Figure 10 shows the globally and annually averaged temperature time series from the base GEOSCCM and 2D model simulations as indicated. As an observational reference, we also show the NCEP reanalysis and reanalysis-2 data at 20 km for 1958-2009, and the new NASA Modern Era Retrospective-analysis for Research and Applications (MERRA) meteorological analyses (see the wesite: http://gmao.gsfc.nasa.gov/research/merra/) for 1979-2009 at 40 and 60 km. To match the early years of the data and to account for the systematic differences between the models, the model curves have been offset as listed in the Figure 10 caption. Although there is interannual variability in the data, the base models simulate the general rate of stratospheric cooling seen in the observations. Also, the 2D and GEOSCCM base simulations have similar rates of cooling throughout 1950-2100, consistent with the fact that both models utilize the same IR radiative transfer schemes. Further model temperature trend comparisons are discussed in Appendix B (Figures B2 and B3).

Following the time change in the surface boundary conditions (Figure 1), the 2D simulated temperature changes in Figure 10 are significantly larger after ~1970 compared with the 1850-1970 time period. Prior to 1950, the temperature changes in the stratosphere are due almost entirely to the

CO_2 loading, with negligible impacts due to ODS and N_2O loading. The temperature changes for 1850-1950 from the 2D base run are mostly linear at 20, 40, and 60 km, and are -0.05K/decade, -0.14K/decade, and -0.17K/decade, respectively. These magnitudes are generally consistent with the GISS modelE results reported in Hansen et al. [2007].

As discussed in previous studies, ODS loading and the corresponding reduction in ozone heating have a large impact on the temperature changes in the recent past, maximizing in the lower and upper stratosphere as seen in the vertical profiles in Figure 11 (top). By 2100, CO_2 cooling dominates the total temperature change throughout the stratosphere, and is significantly larger than the warming caused by the reduced ODS loading (Figure 11, bottom).

The temperature impact of N_2O caused by the associated NO_x-ozone depletion maximizes at 30-40 km but is relatively small (-0.05 K/decade in Figure 11), corresponding to a cooling of -0.7K from 1850-2100 at 40 km (green curve in Figure 10, middle).

Increases in CH_4 induce temperature changes via several mechanisms. Below $\sim$18 km, there is a slight warming (Figure 11) caused by the combination of the direct infrared radiative effect of CH_4 and the indirect radiative effect of the resulting ozone increases in the troposphere and lower stratosphere [e.g, Portmann and Solomon, 2007]. In the stratosphere, increases in CH_4 lead to warming via the increases in ozone caused by the reduction of active chlorine by the the reaction $CH_4 + Cl \rightarrow HCl + CH_3$. Increases in CH_4 also lead to cooling in the stratosphere and mesosphere via the increases in water vapor. In the global average, the combination of these processes results in a net cooling above $\sim$20 km in Figures 10-11.

In the lower mesosphere, the cooling effect of the CH_4-induced H_2O increases becomes large and is comparable to the CO_2 cooling during 1850-2000 at 60 km (Figure 10, top). By 2055, the CH_4-induced cooling is roughly half that due to the CO_2 changes at 60 km in Figure 10. We note also that the future CH_4-induced temperature changes in Figure 11 (bottom) are significantly smaller by 2095 compared to 2055, following the decrease in the CH_4 surface boundary condition during the latter half of the 21^{st} century in the A1B scenario (Figure 1).

5 Age of Air

Previous studies have shown that GHG loading and ozone depletion impact the stratospheric circulation and age of air [e.g., Butchart and Scaife, 2001; Austin and Li, 2006; Butchart et al., 2006; Kodama et al., 2007; Garcia and Randel, 2008; Li et al., 2008; Oman et al., 2009]. Although observations show little or no age trend over the past 30 years in the NH above 24 km [Engel et al., 2009], simulation of a general decrease in age through the 21^{st} century appears to be robust among coupled chemistry-climate models [SPARC CCMVal, 2010].

Here we briefly examine how the individual source gas perturbations used in this study impact the model age of air simulations. This is summarized in Figure 12 (top panel), which shows time series of global and annually averaged age of air at 25 km from the various model simulations as indicated. These results are representative of altitudes above $\sim$20 km. There is significant interannual variability in the GEOSCCM time series which is comprised of three simulations covering the periods 1950-2004, 1971-2052, and 1996-2100. However, the base 2D and GEOSCCM simulations have similar rates of decrease in mean age over the 1960-2100 time period.

As with ozone and temperature, the 2D-simulated changes in mean age are relatively small prior to 1950, with CO_2 loading accounting for about half of the total decrease of 0.1 years from 1860-1950. The base simulated age decreases much more rapidly after $\sim$1970 when the impacts of CO_2 and ODS loading become large and act in the same direction. The total age decrease is 0.3 years from 1980-2005, with 65% of this change due to ODS loading, 25% due to CO_2, and 10% caused by N_2O and CH_4 changes. This dominance of the ODS loading is consistent with the GEOSCCM analysis of Oman et al., [2009]. Figure 12 (top) also shows a 2D-ODS only simulation with all heterogeneous chemical processes turned off, i.e., no ozone hole is simulated (blue dashed-dotted line). This simulation shows only small mean age change due to gas-phase chlorine-ozone destruction, and suggests that most of the ODS effect on the age of air change is due to the ozone hole. Separation of these ODS impacts on mean age is currently being investigated in the GEOSCCM (L. Oman, personal communication).

In the future, the base simulation age decreases less rapidly as the effects of the reduced ODS loading partially offset the CO_2 impacts, with the latter becoming the dominant mechanism after about 2025. By 2100, CO_2 loading accounts for $\sim$75% of the total age change ($\sim$1 year) from 1860. N_2O, CH_4, and the remaining effects of ODS loading have secondary impacts by 2100, with mean age decreases of 0.12, 0.05, and 0.08 years (12%, 5%, and 8% of the total) respectively, from 1860-2100.

Previous studies have attributed the BDC acceleration to increased stratospheric wave driving resulting from changes in the zonal mean winds. These are ultimately due to changes in the temperature distribution induced by SST changes, GHG loading, and polar ozone depletion [e.g., Olsen et al., 2007; Kodama et al., 2007; Garcia and Randel, 2008; Oman et al., 2009]. The 2D model formulation uses parameterizations to account for planetary and gravity wave effects (section A1), and the latitude-height patterns of the long term changes in zonal mean temperature, zonal wind, wave-induced acceleration, lower stratospheric tropical upwelling, and age of air are generally similar to those in WACCM3 and GEOSCCM [Garcia and Randel, 2008; Oman et al., 2009].

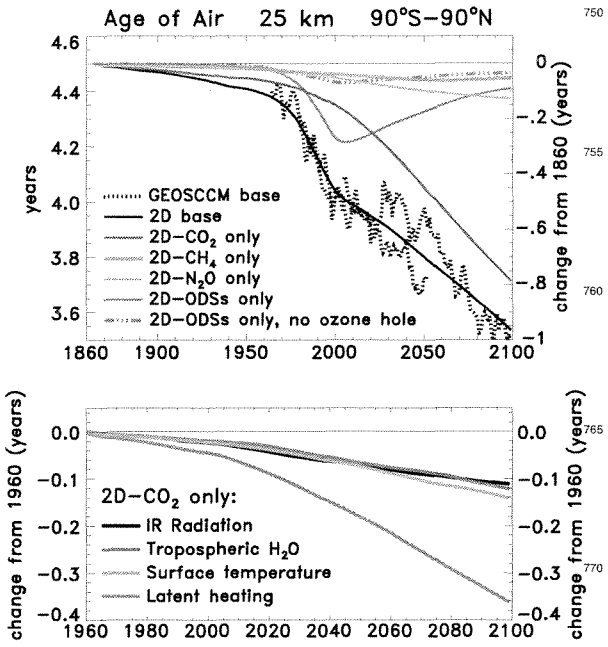

Fig. 12. Global and annually averaged age of air at 25 km. (Top) Time series for 1860-2100 from the base simulations (all source gases varied time dependently) of the GEOSCCM (black dotted lines) and 2D model (black solid lines). Also shown are 2D simulations in which only certain source gases are varied time dependently as indicated. The blue dashed-dotted line is a 2D-ODS only simulation with all heterogeneous chemical reactions turned off so that no ozone hole is simulated. The right hand axis shows the change relative to 1860. The GEOSCCM time series is comprised of three simulations, which use somewhat different SSTs, for the time periods 1950-2004, 1971-2052, and 1996-2100 (the first 8-10 years of each simulation have been removed to allow for spin-up). For visual clarity and to account for a systematic offset between the models, we have added .3 years to the GEOSCCM curves. (Bottom) Time series for 1960-2100, relative to 1960, from several 2D-CO_2 only simulations which use time dependent perturbations for the different processes indicated as discussed in Figure A1. The sum of the curves in the bottom panel equals the 2D-CO_2 only simulation (red curve) in the top panel. See text for details.

Therefore, it appears that the same basic characteristics of the CCM-simulated BDC and age of air changes are also present in the 2D model.

The CO_2 perturbation shown in Figure 12 (top) modifies the model temperature field via the direct IR effect, and through changes in surface temperature, latent heating, and tropospheric H_2O which are parameterized from the GEOSCCM (Figure A1). These processes are likely due, at least in part, to the response of the GEOSCCM hydrological cycle to long term SST changes. To examine the relative contributions of these processes to the 2D model age evolution, we ran four additional time dependent CO_2-only simulations in which the surface temperature, latent heating, tropospheric H_2O, and direct IR effect were varied individually, with the other CO_2 effects held fixed at 1960 levels. The resulting age of air changes are shown in the bottom panel of Figure 12, relative to 1960 values (we restrict our analysis here to the 1960-2100 time period when the age changes are largest). The increase in latent heating has by far the largest impact, contributing ~50% (−0.36 years) of the total CO_2-induced mean age change (−0.73 years) from 1960-2100. The impacts due to tropospheric H_2O (purple line), surface temperature (green line), and the direct IR radiative effect (black line) are all a factor of ~3 smaller, with age changes of −0.1 to −0.14 years from 1960-2100. The magnitude of the direct IR effect is similar to the GEOSCCM results reported in Oman et al. [2009]. Note that the sum of the four curves in the bottom panel equals the full CO_2-only simulation (red curve) in the top panel.

The ODS, N_2O, and CH_4 perturbations shown in Figure 12 (top) modify the 2D model temperature field via the small direct IR radiative effect (lower atmospheric warming) and the larger indirect radiative effects caused by the induced ozone and H_2O changes. These temperature changes modify the model zonal wind, wave driving, and BDC, which in turn drive the age of air changes shown in Figure 12 (top).

The impact in the ODS-only simulation (blue solid curve) is driven mainly by the strong cooling trend during 1970-2000 associated with the ozone hole (Figure B2), which induces a positive trend in zonal wind (increasing westerlies) at high SH latitudes. The accompanying trends (enhancements) in the planetary wave driving and BDC acceleration decrease the age of air. For the ODS-only simulation without the ozone hole (blue dashed-dotted curve), the ozone loss and cooling is confined to the upper stratosphere globally, with only small positive trends in zonal wind and wave driving at midlatitudes of both hemispheres, resulting in small BDC acceleration and age of air changes in Figure 12.

6 Photochemical Lifetimes

Given the significance of the long term stratospheric changes caused by GHG and ODS loading, it is useful to examine how these changes impact the modeled photochemical lifetimes of certain compounds. The lifetime is important in determining the length of time over which a molecule of a substance will have a significant impact on ozone depletion or global warming, and in deriving surface mixing ratio boundary conditions from emissions estimates for use in atmospheric models [Kaye et al., 1994]. The lifetime is computed

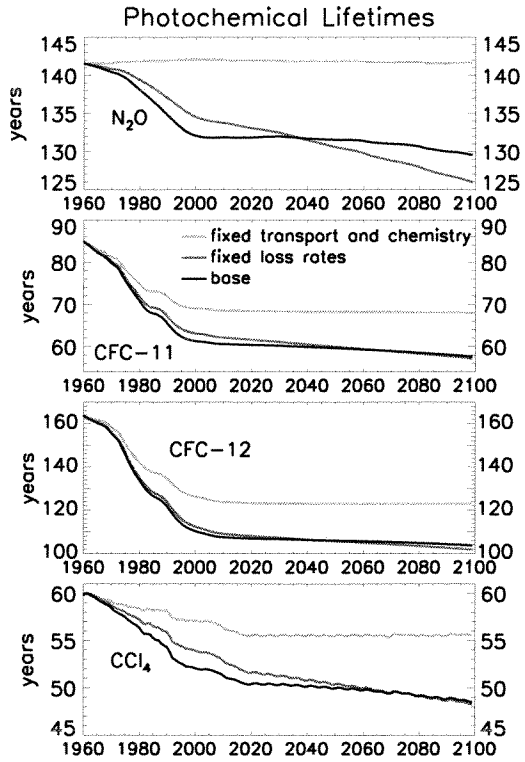

Fig. 13. Time series for 1960-2100 of the photochemical lifetimes for N_2O, CFC-11 ($CFCl_3$), CFC-12 (CF_2Cl_2), and CCl_4 from the base 2D model simulation (black lines). The red lines are from the same base simulation except with the loss rates of N_2O, CFC-11, CFC-12, and CCl_4 fixed at seasonally repeating 1960 values. The green lines are from a simulation using all chemistry and transport fixed at seasonally repeating 1960 values illustrating the effect of the changing atmospheric burden.

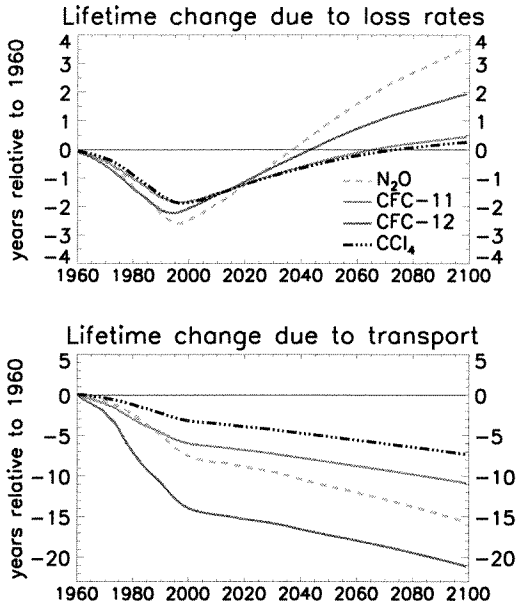

Fig. 14. (Top) The difference between the base and fixed loss rate simulations (black lines minus red lines in Figure 13), illustrating the lifetime changes due to the changing loss rates. (Bottom) The difference between the fixed loss rate and fixed chemistry and transport simulations (red lines minus green lines in Figure 13), showing the lifetime changes due to changes in transport.

as the atmospheric burden (total number of molecules) divided by the loss rate, both of which are vertically integrated and globally/annually averaged. We have recently shown the impact of new photolysis cross sections on the model-computed lifetime of CCl_4 [Rontu Carlon et al., 2010]. Here we examine the time dependence of the lifetimes of various compounds in more detail.

Figure 13 (black lines) shows the modeled lifetimes of N_2O, CFC-11 ($CFCl_3$), CFC-12 (CF_2Cl_2), and CCl_4 from the base 2D simulation. We restrict our analysis here to the 1960-2100 time period since the CFC lifetimes are not well defined prior to 1960 given that emissions began in the late 1930s-1940s. While this is not a problem for N_2O given it's significant natural source, the computed N_2O lifetime decrease from 1860-1960 is small (143-141 years), consistent with the small age of air decrease shown in Figure 12.

The present day lifetimes shown in Figure 13 (132, 61, 108, and 51 years, respectively, for N_2O, CFC-11, CFC-12, and CCl_4), are older than those cited in WMO [2007, 2011] and IPCC [2007]: 114, 45, 100, and 26 years. For CCl_4, the older lifetimes shown here do not include soil or ocean loss processes. Updated lifetimes for CFC-11 and CFC-12 computed from various models (including the 2D model) were presented in Douglass et al. [2008]. That study illustrated a strong dependence of lifetime on the modeled circulation and age of air, and showed that models with realistic age of air simulated a relationship between mean age and the fractional release of CFC-11 and CFC-12 that compared well with observations. We note that the present 2D model compares well with the age of air derived from observations in Figure B4.

Figure 13 (green lines) also shows a simulation in which the time dependent loading of N_2O, CFC-11, CFC-12, and CCl_4 impacts only the atmospheric burden used to compute the lifetimes, while the model transport and chemistry remain

fixed at seasonally repeating 1960 values. This illustrates the effect of the changing burden on the computed lifetimes. As the surface mixing ratio of a substance increases with time, an increasing fraction of the total atmospheric burden resides in the stratosphere where it is lost, as opposed to the troposphere where the loss is zero, and this results in a decrease in the computed lifetime, i.e., the lifetime has not reached equilibrium with the increasing surface boundary conditions [e.g., see Kaye et al., 1994]. For the CFCs, emissions began in the late 1930s-1940s and ramped up quickly during the following decades [Butler et al., 1999], so that there is a large impact of the increasing burden on the lifetimes prior to $\sim$1990. Atmospheric loading of CCl_4 began $\sim$1900 so that the influence of the increasing burden on the lifetime is small by 1960. This effect on the lifetimes of the CFCs and CCl_4 then levels off as the burdens slowly decrease after 2000, i.e., the lifetime has reached equilibrium with the boundary conditions. N_2O has a significant natural source with a slow increase throughout 1960-2100 due to anthropogenic activity (Figure 1), so that the changing burden has little or no impact on the computed lifetime throughout the time period.

The lifetimes are also controlled by the loss rates and the rate of transport of a species through the stratospheric loss region. The loss rates (photolysis and reaction with $O(^1D)$) are impacted by the overhead burden of ozone, and the transport rates are modified via changes in the BDC as discussed previously. Both of these processes incur long term changes via the ODS and GHG loading.

The red curves in Figure 13 are the same as the base simulation except with the loss rates of N_2O, CFC-11, CFC-12, and CCl_4 fixed at seasonally repeating 1960 values. The effect of the changing loss rates is then isolated by taking the difference between the base and fixed loss rate simulations (black lines minus red lines), i.e., the residual is that due to only the changing loss rates. The results are shown relative to 1960 in Figure 14 (top) and reveal small impacts for all four species. These differences approximately follow the changing overhead burden of ozone, with lifetime decreases of $\sim$2 years (i.e., loss rate increase) for all species from 1960-2000 as ozone decreases due to ODS loading. As future ozone increases with reduced ODS and increased CO_2, the impact of the loss rates during 2000-2100 increases the lifetimes by 6 years for N_2O, 4 years for CFC-12, and 2 years each for CFC-11 and CCl_4. These changes are all $<4\%$ over the 1960-2100 time period. This small impact of the changing loss rates was also reported in Douglass et al. [2008].

The effect of the changing BDC is isolated by taking the difference between the fixed loss rate and fixed chemistry and transport simulations (red lines minus green lines), i.e., the residual is that due to only the changing transport. These results are shown in the bottom panel of Figure 14, again relative to 1960. The lifetime decreases are largest during 1960-2000 when the BDC acceleration is fastest (Figure 12), with less pronounced decreases after 2000 as the BDC accelerates more slowly. The net lifetime reductions for 1960-2100 due to the changing BDC are all 11-13%: 16 years for N_2O, 11 years for CFC-11, 21 years for CFC-12, and 7 years for CCl_4.

7 Summary and Conclusions

In this paper we use an updated version of our GSFC 2D coupled model to study long term stratospheric changes caused by source gas loading for the 250-year time period, 1850-2100. We use numerous sensitivity simulations in which the ODSs, CO_2, CH_4, and N_2O are varied individually to separate the relative roles of these gases in driving long term changes in ozone, temperature, and age of air. We also compare the 2D model with global ozone and temperature changes observed during the recent past, and with simulations from the GEOSCCM to illustrate that the updated 2D model captures the basic processes that drive long term stratospheric changes. A detailed description and evaluation of the model are provided in the Appendicies.

For long term changes in ozone, the impacts due to ODS, CO_2, CH_4, and N_2O loading all play important roles in different regions of the atmosphere. GHG loading becomes more important in determining future ozone concentrations as the ODS loading diminishes through the 21^{st} century. CO_2 cooling increases upper stratospheric ozone via reduction in the temperature dependent loss rates. CO_2 loading also leads to acceleration of the BDC which redistributes ozone in the lower stratosphere, with less (more) ozone in the tropics (extratropics). The net CO_2 impact on total ozone is a decrease in the tropics and an increase in the global average and at midlatitudes, with a larger enhancement in the NH. For 1850-2100, CO_2 loading has the largest individual impact on global ozone in the upper stratosphere and on the total column, causing increases of 20% and 4.2%, respectively. N_2O loading and the subsequent increase in the NO_x ozone loss maximizes near 35 km ($\sim$0.5%/decade), with a global total column decrease of -2.7% from 1850-2100.

Methane loading impacts ozone via several processes, and we illustrate the sensitivity of these processes in determining the net result on ozone. The simulations, which use fixed tropospheric NO_y, reveal that CH_4 loading leads to a net increase in total ozone at all latitudes throughout 1850-2100. Global total ozone increases by 2-2.5% from 1850 to the latter half of the 21^{st} century due to CH_4 loading. However when coupled with time dependent ODS changes, the methane impact on ozone for present day conditions is nearly a factor of two larger (+6 DU) compared to the +3 DU response calculated with very low (1850) levels of Cl_y.

In the lower mesosphere, the CH_4-induced HO_x-ozone loss dominates the ozone time dependence. Our simulations reveal that this process resulted in significant ozone reductions prior to 1960, so that one-third of the total decrease in ozone during 1850-2050 occurred by 1960.

In the stratosphere prior to 1960, the simulated ozone changes are relatively small, but are not insignificant. ODS emissions, primarily due to carbon tetrachloride, cause 1% depletion in global total ozone from 1860-1960, with the vast majority of this occuring after ~1920. From 1860-1960, increasing CO_2 loading results in ozone increases of 2% in the upper stratosphere and 0.5% in the total column, with CH_4 and N_2O causing total ozone changes of +0.75% and −0.5% respectively, during this period. The net result is a broad ozone maximum during the 1920s-1930s, as the CO_2 and CH_4-induced ozone increases outpace the ozone losses caused by N_2O and CCl_4 emissions. This preceeds the decline in ozone driven mainly by ODS loading, which becomes much more rapid after ~1970.

We also present a quantitative analysis of the steady state impacts of GHGs on ozone for 1850, 1950, 2000, and 2100 atmospheric conditions. These calculations have a significant dependence on the background conditions, reflecting saturation effects as well as the chemical interactions of the perturbations. Using the ozone depletion potential (ODP) concept for GHGs, we compute present day ODP values of +0.019 (N_2O), −0.00065 (CH_4), and −0.0039 (CO_2), relative to CFC-11. To more easily interpret the relative impacts of the GHGs on ozone, we also derive steady state sensitivity factors in terms of the mixing ratio change of each GHG. These calculations reveal that based on the A1B scenario, CH_4 had the largest impact on ozone for year 2000 conditions, owing to it's strong coupling with Cl_y. However, CO_2 is projected to have the largest impact by 2100, and will have twice the magnitude of the N_2O impact.

The simulated changes in stratospheric temperature for 1850-2100 are mostly controlled by CO_2 cooling, with the reduced ozone heating caused by ODS loading also playing an important role from ~1980 through the first half of the 21^{st} century. The impact of CH_4 and N_2O loading are relatively small below ~45 km. However, the cooling due to CH_4-induced H_2O increases becomes significant above ~50 km, and the resultant temperature changes are comparable to those induced by the ODS and CO_2 loading.

In the 2D model, the long term changes in surface temperature, latent heating, and tropospheric H_2O are parameterized based on the GEOSCCM simulations and the CO_2 loading. These processes are likely due, at least in part, to the response of the GEOSCCM hydrological cycle to long term SST changes. Parameterization of these processes enables the 2D model to simulate long term changes in the BDC and age of air which are consistent with the GEOSCCM. Changes in GHG and ODS loading ultimately impact the BDC and age of air through changes in the radiative and temperature distributions. We estimate that changes in ODS concentrations account for 65% of the mean age decrease from 1980-2005, with 25% due to CO_2 loading, and 10% due to CH_4 and N_2O. Our simulations also indicate that the BDC and age changes caused by ODS loading are mainly due to the formation of the ozone hole. CO_2 loading becomes the dominant source of mean age change after ~2025, and explains ~75% of the total age reduction (1 year) from 1860-2100, with 12% and 5% explained by N_2O and CH_4 loading, respectively.

We also examined the time dependent photochemical lifetimes of N_2O, $CFCl_3$, CF_2Cl_2, and CCl_4, and found that the impact of the BDC acceleration is significant, and causes the lifetimes to decrease by 11-13% from 1960-2100. The impact of the changing loss rates is generally small and follows the time dependent changes in stratospheric ozone via the changes in photolysis and $O(^1D)$. This effect decreases the lifetimes by ~2 years from 1960-2000, and increases the lifetimes by 2-6 years (3-4%) from 2000-2100. The model calculations also allow us to separate these geophysical impacts on the lifetimes from the artifacts caused by the disequilibrium between the rapidly increasing atmospheric burden and the stratospheric loss.

Appendix A

GSFC Coupled 2D Model

The GSFC 2D coupled chemistry-radiation-dynamics model was originally discussed in Bacmeister et al., [1995] and has been frequently used in stratospheric assessments [WMO, 2007], and studies pertaining to the chemistry-climate coupling of the middle atmosphere [e.g., Rosenfield et al., 1997; Rosenfield et al., 2002]. While this model was not included in the recent CCMVal activity [SPARC CCMVal, 2010], several of the model components are very similar to those used in the GEOSCCM which was evaluated in CCMVal. These components include: the infrared radiative transfer scheme [Chou et al., 2001]; the photolytic calculations [Anderson and Lloyd, 1990; Jackman et al., 1996]; and the microphysical model for PSC formation [Considine et al., 1994]. As discussed in Fleming et al. [2007], the model now uses an upgraded chemistry solver that computes a full diurnal cycle for 35 fast chemical constituents. This scheme was shown to be in good agreement with photochemical steady state box model calculations [Park et al., 1999]. The latest Jet Propulsion Laboratory (JPL) recommendations are used for the photolytic cross sections and reaction rate constants [Sander et al., 2006].

The model domain extends from the ground to approximately 92 km. The chemistry calculations are done on a grid resolution of 4° latitude by 1 km altitude. We have found that for most applications, the model radiation and dynamics calculations can be adequately done on a somewhat coarser grid of ~ 4.9° latitude by 2 km altitude. Using a finer resolution only adds to the computational burden but does not improve the model dynamical simulations.

We have recently made extensive upgrades to the model solar radiation and dynamical modules, which are described in the following sections. An evaluation of the model temperature and transport are then provided in Appendix B.

A1 Wave Parameterizations

The horizontal mixing (K_{yy}) and momentum deposition due to dissipating planetary waves is computed using a linearized parameterization similar to that described by Garcia [1991]. Previously, the parameterization used a surface boundary condition based on a representation of the topographic forcing of planetary waves. It was necessary to include adjustable amplitude efficiency factors for each wave number to obtain reasonable seasonal variations of the zonal winds and chemical fields [Rosenfield et al., 1997]. In the present model, this lower boundary condition is based on a geopotential height climatology for 750 mbar as a function of latitude and season, derived from the National Centers for Environmental Prediction (NCEP) reanalysis-2 data [Kistler et al., 2001] averaged over 1979-2007. This provides a more complete representation of the lower boundary forcing of planetary waves, e.g., land-ocean contrasts, in addition to the topographic forcing. We solve for planetary zonal wave numbers 1-4. Compared to that obtained previously, the new methodology provides more realistic model simulations of planetary wave drag and mixing with no artificial wave amplitude adjustment factors necessary.

The model also includes the off-diagonal eddy diffusion of constituents (K_{yz}), following the methodology used in our GSFC 2D fixed transport model. This follows the assumption that horizontal eddy mixing is directed along the zonal mean isentropes, and projects the K_{yy} mixing rates onto isentropic surfaces [Plumb and Mahlman, 1987; Newman et al., 1988].

The momentum deposition due to gravity wave breaking in the mesosphere is parameterized using a ray tracing calculation for waves with non-zero phase speeds, and a cubic drag law for zero-phase speed mountain waves [Bacmeister et al., 1995]. This enables the gravity wave momentum flux to be interactive with the evolution of the zonal mean flow. However to obtain proper tracer simulations, we found it necessary to specify the model vertical eddy diffusion rates (K_{zz}), which are taken from the GSFC 2D fixed transport model as a function of latitude, height, and season [Fleming et al., 2007]. For the upper stratosphere and mesosphere, these are based on the gravity wave parameterization originally developed by Lindzen [1981] and modified by Holton and Zhu [1984]. For the troposphere and lower stratosphere, K_{zz} is based on the zonal mean temperature lapse rate as computed from a multi-year average of NCEP reanalysis-2 data.

A2 Radiative Transfer

For the absorption of solar radiation in the ultraviolet and visible, we now compute the heating rates consistently with the model incident solar flux and photolysis calculations [Jackman et al., 1996]. These are computed over a full diurnal cycle with a much finer spectral resolution compared to the broad band calculations used previously [Strobel, 1978; Chou and Suarez, 1999]. These heating rate calculations have the further advantage of utilizing the most current recommendations for the photolytic cross sections [Sander et al., 2006]. This new methodology also gives model temperatures that are in somewhat better agreement with observations.

For ozone, the heating rate in this way is computed by [e.g, Brasseur and Solomon, 1986]:

$$\frac{dT}{dt} = \frac{1}{\rho C_P}[O_3]\int_\lambda \sigma_{(O_3)} F_{s,\lambda} d\lambda \qquad \text{(A1)}$$

where ρ is the total atmospheric density, C_P is the specific heat of dry air at constant pressure, $[O_3]$ is the ozone number density, λ is the wavelength, $\sigma_{(O_3)}$ is the ozone absorption cross section, and $F_{s,\lambda}$ is the incident solar flux (enhanced or reduced) as a function of wavelength at each model grid point. In addition to ozone heating, we also include the heating due to absorption by O_2, which is important in the mesosphere, and NO_2 which is of secondary importance in the middle stratosphere. For these calculations, we assume that all of the solar radiation absorbed is immediately realized as thermal energy. This is a good approximation below ~80 km, i.e., the region of interest for the current study, where the chemical recombination of $O(^3P)$ is very fast [e.g, Brasseur and Solomon, 1986].

We also include the minor absorption of solar radiation by ozone in the infrared, and by water vapor in the infrared and visible based on the parameterization of Chou and Suarez [1999]. For these calculations, we use surface reflectivity values as a function of latitude and season based on the TOMS climatology compiled by Herman and Celarier, [1997].

For the thermal infrared radiative transfer, we use the parameterization of Chou et al. [2001], which is the same as that used in the GEOSCCM. This includes the contributions due to O_3, CO_2, H_2O, CH_4, N_2O, CFC-11, CFC-12, and HCFC-22. For both the solar and thermal IR calculations, the 2D model includes zonally averaged cloud parameters based on a multi-year average of output from the Whole Atmosphere Community Climate Model version 3 (WACCM3) [e.g., Garcia et al., 2007].

A3 Model Treatment of Longitudinal Variations

Previously, the model-generated zonal mean temperatures were used to compute the gas phase and heterogeneous reaction rates. In the new model version, reaction rates are now computed using a longitudinal temperature probability distribution which is generated from the model-computed planetary wave fields for zonal waves 1-4 (section A1). The rates for the reactions at each model grid point are computed once per day by summing the rates computed for each temperature in the distribution weighted by the probability of occurrence of that temperature. Using the temperature probability distribution instead of the zonal mean temperature is especially important for the heterogeneous chemical reactions as these can have significant non-linearities in temperature.

For the calculation of polar stratospheric cloud (PSC) formation, we utilize the parameterization described in Considine et al. [1994], using longitudinal temperature probability distributions derived from the NCEP reanalysis-2 data averaged over 1979-2006. This climatological average distribution is used for all years in the simulations. This methodology does not allow for the interaction between PSC formation and the chemical/dynamical time evolution of the model stratosphere. However given the strong temperature non-linearity of PSC formation, we found it necessary to use the observed temperature distributions rather than the model temperatures to properly simulate PSC formation.

A4 Tropospheric Parameterizations

Accounting for the hydrological cycle and surface boundary layer processes is important to properly simulate the dynamical and chemical distributions of the troposphere and lower stratosphere. Since the 2D model framework is inadequate to simulate most tropospheric processes interactively, we specify the surface temperature, tropospheric water vapor and latent heating. As described in the following, we first generate monthly and zonal mean climatologies of these parameters, and then add on long term changes parameterized in terms of the atmospheric CO_2 loading.

The surface temperature seasonal cycle as a function of latitude is based on the NCEP reanalysis-2 data averaged over 1979-2006. Tropospheric latent heating as a function of latitude, height, and season is based on a multi-year average of output from WACCM3 simulations. The model water vapor seasonal cycle in the upper troposphere (12-16 km) is based on the UARS reference atmosphere (UARSRA) compiled by Randel et al., [2001]. Below 12 km, water vapor is derived from a 21 year average (1981-2001) of relative humidity data from the European Center for Medium Range Weather Forecasts (ECMWF) updated reanalyses (ERA-40). Values from the UARSRA and ERA-40 data sets are functions of latitude, height, and season and are blended over several pressure levels to obtain a smooth transition in the vertical. Water vapor everywhere above the tropopause is computed in the 2D model (see Figure B6).

In addition to the seasonal variations, the surface temperature, tropospheric water vapor and latent heating undergo substantial long term changes as simulated by the GEOSCCM. This is illustrated in Figure A1 which shows zonally averaged time series of GEOSCCM simulations for 1950-2100 (black curves) at the locations indicated. These time series have been deseasonalized and smoothed to reduce the interannual variability of the GEOSCCM. These long term changes are highly correlated with the time dependent surface boundary condition of CO_2 (bottom panel) and are likely a response to the warming of the troposphere and sea surface temperatures caused by the increased atmospheric CO_2 loading. To represent these long term changes in the 2D model, we compute a sensitivity factor to the CO_2 boundary condition for each parameter at each model grid point. The time dependent value of each parameter is then determined by the CO_2 concentration at each time step multipled by the sensitivity factor. As depicted by the red curves in Figure A1, this smoothly-varying fit to the CO_2 boundary condition allows us to remove the unwanted artifacts of the GEOSCCM interannual variability. This also allows us to extrapolate these quantities to years prior to 1950 based on the CO_2 loading, assuming the same sensitivity to CO_2 as for 1950-2100. The orange shading in Figure A1 shows the climatological seasonal cycle for each parameter added onto the long term variation for input into the 2D model.

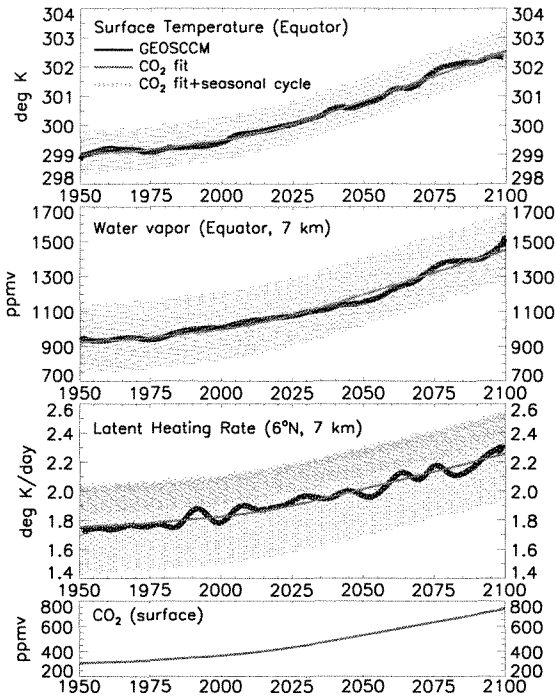

Fig. A1. Time series for 1950-2100 of zonally averaged and deseasonalized surface temperature, water vapor mixing ratio, and latent heating from the GEOSCCM (black curves), and the corresponding fits to the surface CO_2 boundary condition (red curves) for the locations indicated. Inclusion of the seasonal cycle to the CO_2 fits is depicted by the orange shading. The surface CO_2 boundary condition is shown in the bottom panel. See text for details.

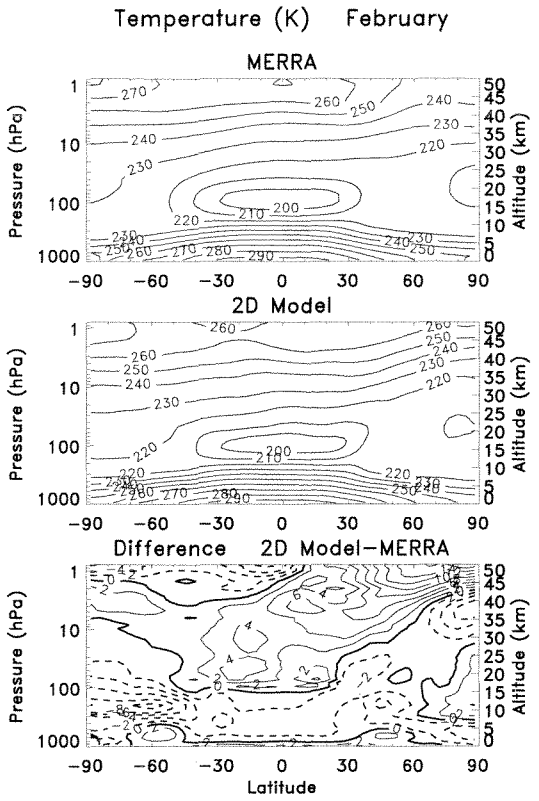

Fig. B1. Latitude-height cross-sections of the February monthly mean temperature (K) from the MERRA data (top), 2D model simulation (middle), and the difference, model minus MERRRA (bottom panel), all averaged over 1979-2009. The contour intervals are 10K for the top and middle panels and ±2 K for the bottom panel.

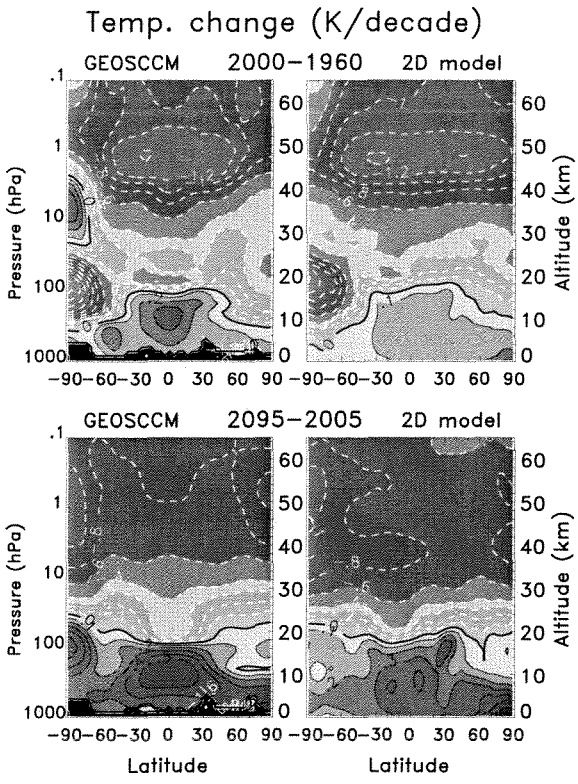

Fig. B2. (Top panels) Annually averaged temperature trend for 2000-1960 from the GEOSCCM (left) and 2D model (right) base simulations (all source gases varied time dependently). The trends are derived from linear least squares fits to the annually averaged time series. (Bottom panels) As in the top panels except for the 2095-2005 temperature difference (K/decade) using 10-year averages centered on 2095 and 2005 to reduce the effects of interannual dynamical variability in the GEOSCCM. The contour interval is ±0.1 K/decade.

Appendix B

2D Model Temperature and Tracer Comparisons

In this Appendix, we provide an evaluation of the 2D model transport fields by comparing the simulations with observations of several tracers including ozone. We also evaluate the model temperature simulations (climatology and trends).

B1 Temperature

The model temperature field for February is shown in Figure B1, along with the MERRA meteorological analyses (section 4), both averaged over 1979-2009. The largest model differences (bottom panel) occur at high SH latitudes in the upper troposphere (−10K), and in the upper stratosphere at high NH latitudes (+14K). However overall, the model is in reasonable agreement with the MERRA data, as the model differences are mostly within ±5K.

The past and future temperature changes from the 2D model and GEOSCCM are shown in Figure B2. The 2D model captures most of the latitude-height variations simulated in the GEOSCCM. The main discrepancies occur at high latitudes where the 2D model somewhat underestimates the large temperature changes simulated by the GEOSCCM associated with the ozone hole, i.e., past cooling and future warming. Also, the GEOSCCM simulates a mid-upper stratospheric warming at high SH latitudes for 1960-2000, which was shown to be a dynamical response to the ozone hole [Stolarski et al., 2006]. The 2D model simulates this feature only very weakly (top right). These discrepancies are likely due to the 2D model not fully resolving the large zonal asymmetries characteristic of the polar region, as well as the known high ozone bias at high latitudes in the GEOSCCM

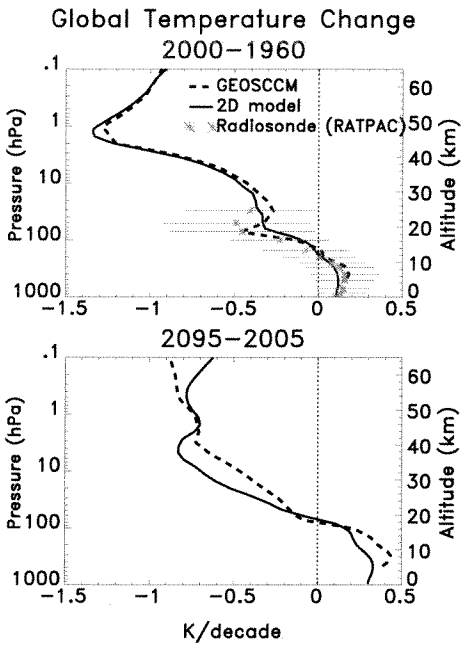

Fig. B3. As in Figure B2, except for the global (90°S-90°N) average profiles. The top panel includes the trend derived from radiosonde data (RATPAC-A) [Free et al., 2005].

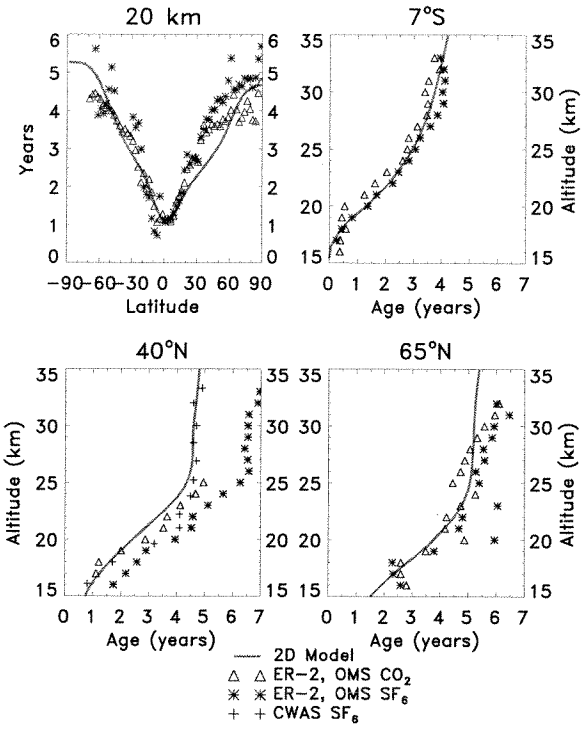

Fig. B4. Age of air at 20 km derived from ER-2 aircraft measurements of SF_6 (asterisks) and CO_2 (triangles), and vertical profiles of the age of air derived from balloon measurements of SF_6 (asterisks, plus signs) and CO_2 (triangles) at the latitudes indicated. Ages derived from these measurements have been adapted from Hall et al. [1999]. Also shown are simulations from the 2D model (red line). The age is taken relative to the tropical tropopause.

[Pawson et al., 2008].

The corresponding global average vertical profiles (Figure B3) also show good agreement between the 2D model and GEOSCCM as well as radiosonde data for 1960-2000 from the Radiosonde Atmospheric Temperature Products for Assessing Climate (RATPAC-A) [Free et al., 2005]. We note that the global average GEOSCCM stratospheric temperature trends were also found to be in reasonably good agreement with those derived from SSU and MSU satellite data for 1979-1999 [Stolarski et al., 2010].

In the troposphere, the 2D model simulates warming throughout 1960-2100, which is due mainly to the parameterized long term changes in surface temperature and latent heating shown in Figure A1. The magnitude of the warming in the tropics is somewhat underestimated compared with the GEOSCCM in both the past and future (Figure B2), although the 2D-simulated warming over 1960-2000 compares favorably with the radiosonde data in the global average in Figure B3.

B2 Age of Air

Stratospheric age of air is a widely used diagnostic that tests the overall fidelity of model transport [e.g., Hall et al., 1999]. Figure B4 shows the mean age of air at 20 km derived from aircraft measurements of SF_6 (asterisks) and CO_2 (triangles), and a series of vertical profile measurements of SF_6 and CO_2 made from balloon flights in three latitudes zones [e.g., see Hall et al., 1999]. We note that differences in the observations at the middle and higher latitudes may reflect photo-chemical influences on SF_6 which would cause an overestimation in the inferred ages [Hall and Waugh, 1998]. Some of the older age measurements at 65°N may also reflect remnants of the winter polar vortex [Ray et al., 1999].

Figure B4 also shows the age of air derived from the 2D model simulation averaged over the 1990s (red line). The age of air in the model is computed from a "clock" tracer

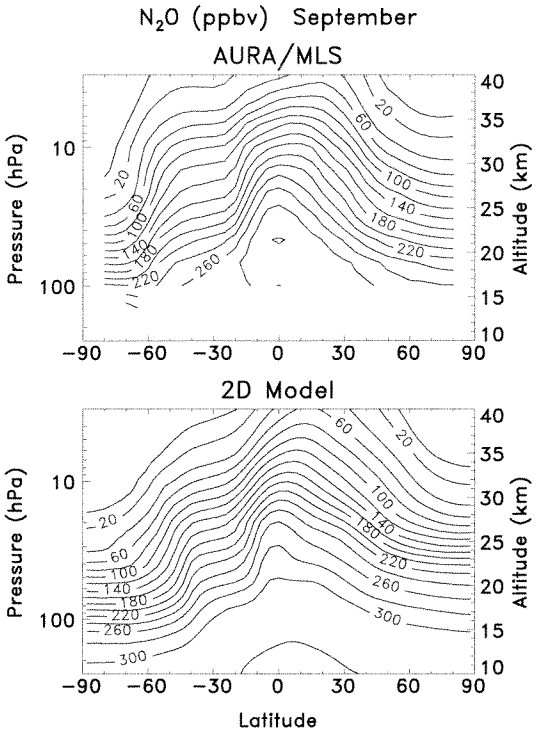

Fig. B5. Latitude-height cross-sections of September N_2O averaged over 2004-2009 from AURA/MLS (top) and the 2D model (bottom). Contour interval is 20 ppbv and includes the 10 ppbv contour.

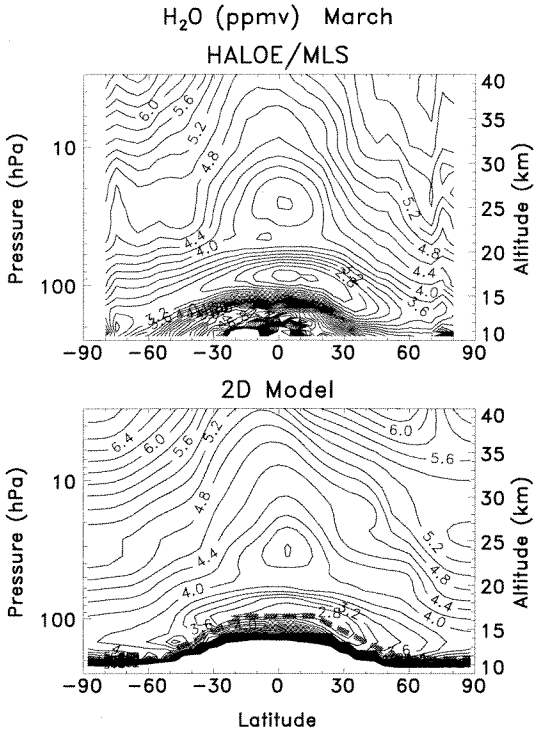

Fig. B6. Latitude-height cross-sections of March H_2O averaged over 1994-2004 from UARS/HALOE (top) and the 2D model (bottom). The top panel includes data from AURA/MLS in the polar regions (averaged over 2004-2009) where HALOE lacks data coverage. Contour interval is 0.2 ppmv. The red dashed line separates the regions where the model H_2O is computed (above) and prescribed to the HALOE climatology (below).

that has a surface boundary condition linearly increasing with time, with no other chemical production or loss. This is essentially identical to the age obtained from simulations of SF_6 or CO_2 as done, for example, in Hall et al. [1999]. The model somewhat underestimates the observed age in the mid-latitude Northern Hemisphere (NH) (see the 20 km and 40°N panels), and at the high latitudes of the NH above 30 km. However for the most part, the model simulates the absolute values and the latitudinal and vertical gradients of the observations fairly well. This illustrates that the model transport rates in the stratosphere, i.e., the relative magnitudes of vertical motion and horizontal mixing, are generally realistic.

B3 N_2O and H_2O

As further evaluation of the model transport, we show latitude-height cross sections of September N_2O from the model and the AURA/MLS data averaged over 2004-2009 (Figure B5), and March H_2O from the model and the UARS/HALOE data both averaged over 1994-2004 (Figure B6). Figure B6 includes data from AURA/MLS in the polar regions (averaged over 2004-2009) where HALOE lacks data coverage. The model shows good overall agreement with the data in reproducing transport sensitive features in the meridional plane, including the horizontal and vertical gradients. For example, the model qualitatively simulates the region of strong horizontal mixing during late winter/early spring at midlatitudes of both hemispheres. This is especially pronounced in the SH during September at 20-40 km in the N_2O field. The model tends to underestimate this mixing in the SH mid-upper stratosphere, as is also seen in the midlatitude vertical profile in Figure B7 (top). Here the model compares well with the MLS N_2O below ~27 km, but underestimates the data above this level, which is due to weaker than observed mixing of high-N_2O air from lower latitudes.

In the Antarctic lower stratosphere, the observed N_2O profile in September (Figure B7, bottom) is mainly a result of de-

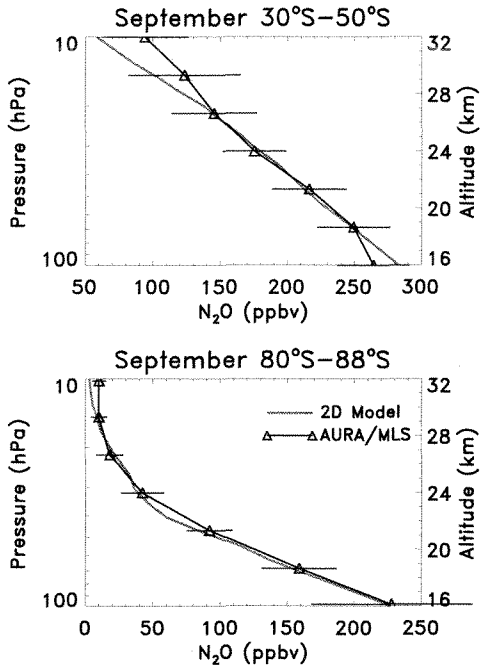

Fig. B7. Vertical profiles of September N_2O at 30°S-50°S (top) and 80°S-88°S (bottom) from AURA/MLS observations (black triangles) and the 2D model (red curve) averaged over 2004-2009. The error bars (1σ) denote the combined effects of measurement uncertainty and interannual variability. The Antarctic MLS profile is adapted from SPARC CCMVal [2010].

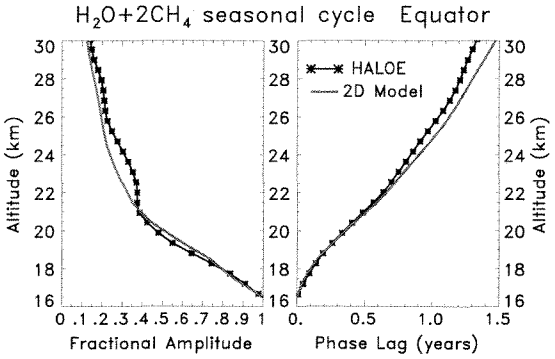

Fig. B8. Equatorial profiles of the amplitude and phase lag of the seasonal cyle in the quantity $H_2O + 2CH_4$ from UARS/HALOE (black asterisks) and the 2D model (red). Amplitudes are relative to the values at 16.5 km, and the phase lag is defined to be zero at 16.5 km. Values are averaged over 1994-2004 for both the data and model.

scent within the vortex occurring throughout the winter, with little influence of air in-mixing from midlatitudes [SPARC CCMVal, 2010]. The good model-data agreement here illustrates that the magnitudes of vortex descent and isolation from midlatitudes in the simulation are generally realistic.

The HALOE H_2O data in Figure B6 indicate strong poleward and downward transport of very dry air from the tropics to midlatitudes just above the tropopause [e.g., Randel et al., 2001]. The model H_2O is set to the HALOE climatology in the upper troposphere, below the red dashed line in Figure B6. Above this level, the H_2O field is computed in the model, and reveals that the model transport is resolving fairly well this strong poleward and downward transport from the tropical tropopause region.

In Figures B5 and B6, the model also resolves the isolation of the tropics in the lower stratosphere, as indicated by strong horizontal gradients in the subtropics, and a region of low water vapor concentrations at 20-30 km over the equator associated with the "tape recorder" signal [e.g., Mote et al., 1996]. This feature reflects the slow upward propagation of the water vapor seasonal cycle from the tropical tropopause, and simulation of this feature provides a good diagnostic of model transport.

Figure B8 shows the amplitude variation and phase lag versus altitude of the seasonal cycle in $H_2O + 2CH_4$ at the equator relative to the tropopause from HALOE data (black asterisks). This quantity is quasi-conserved and accounts for both the H_2O seasonal cycle propagation and the slow photochemical conversion of CH_4 into H_2O in the stratosphere. The amplitude attenuation and phase lag with increasing height reflect the strength in the upwelling of the Brewer-Dobson circulation (BDC) combined with the rate of vertical diffusion and entrainment of air from mid-latitudes [Hall et al., 1999]. The model (red line) shows an increasingly longer phase lag compared with the data above ~27 km, possibly reflecting weaker BDC upwelling in the trop-

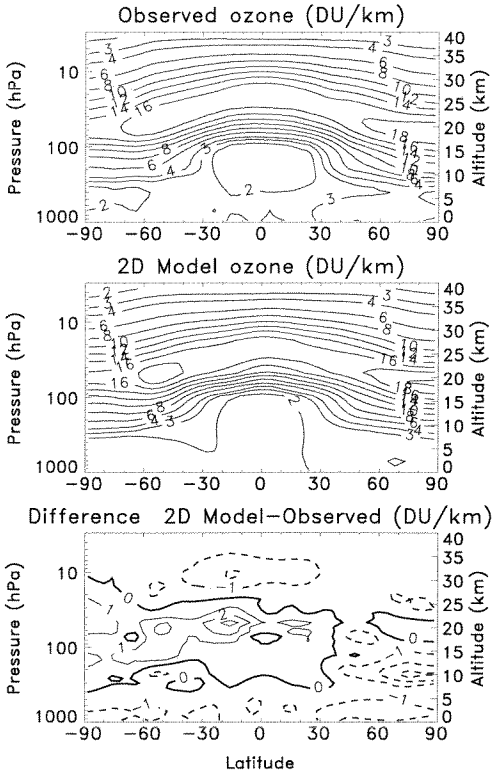

Fig. B9. Latitude-height cross-sections of annually averaged ozone expressed in Dobson Units per kilometer. The observations (top panel) are from the climatology compiled by McPeters et al. [2007] covering the time period 1988-2002. Also shown are the 2D model simulation averaged over 1988-2002 (middle panel), and the difference, model minus observations (bottom panel). For the top and middle panels, the contour interval is 2 DU/km and includes the 3 contour level. For the bottom panel, the contour interval is ±1 DU/km.

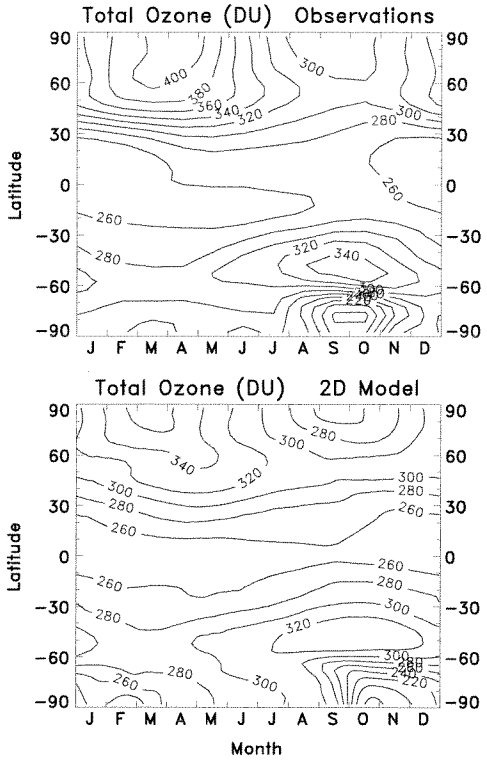

Fig. B10. Month-latitude cross-sections of total column ozone averaged over 1988-2002 from ground-based observations (top panel, updated from Fioletov et al. [2002]) and 2D model simulation (bottom panel). The contour interval is 20 DU.

ical middle stratosphere than indicated in the observations. However overall, the model shows mostly good agreement with the HALOE data in simulating this seasonal cycle propagation. This, combined with the good agreement in the tropical age profile (Figure B4), suggests that the model transport rates in the tropical lower-middle stratosphere appear to be fairly realistic.

B4 Ozone

Figure B9 shows latitude-height cross sections of annually averaged ozone from an observational climatology (top panel), the model (middle panel), and the difference, model minus data (bottom panel) expressed in DU per kilometer. This unit is proportional to the number density per cm^2 divided by a constant, and is a direct measure of the contribution versus altitude to the total column. The climatology is based on a combination of ground based and satellite data covering the time period 1988-2002, as compiled by McPeters et al. [2007]. The model results are also averaged over 1988-2002.

The simulation compares relatively well with the data in most regards. The model qualitatively reproduces the observed latitudinal and vertical gradients in most places, as well as the magnitude of the ozone amounts. There are some regions of small discrepancy; for example at 15-20 km in the SH midlatitudes where the model slightly overestimates ozone, and in the tropics above 30 km associated with the ozone deficit region where the model underestimates ozone [e.g., Jackman et al., 1996]. The model also underestimates ozone at mid-high NH latitudes near 10-15 km which is likely due to excessive horizontal mixing in this region, i.e., in-mixing of low-ozone air from the tropical troposphere. However, these model-measurement differences are now significantly smaller compared with previous model versions.

The corresponding season-latitude sections of total column ozone also averaged over 1988-2002 are shown in Figure B10. The observations are from ground-based measurements updated from Fioletov et al. [2002]. Again the model shows good overall agreement with the data in reproducing the absolute total ozone magnitudes, the latitudinal gradients, and the seasonal variations. The main discrepancy occurs at NH high latitudes where the model tends to underestimate total ozone throughout the year by ~20-50 DU. This reflects the model underestimation of ozone at high NH latitudes in the 10-15 km region seen in Figure B9 (bottom panel).

Acknowledgements. We thank Susan Strahan and Steve Steenrod for providing the GMI CH_4 simulations; Vitali Fioletov for supplying the ground-based total ozone data; and Stacey Frith for providing the near global BUV/SBUV data and derived trends. This work was supported by the NASA Atmospheric Composition: Modeling and Analysis (ACMA) Program.

References

Anderson, D.E., Jr., and Lloyd, S.A.: Polar twilight UV-visible radiation field: Perturbations due to multiple scattering, ozone depletion, stratospheric clouds, and surface albedo, J. Geophys. Res., 95, 7429-7434, 1990.

Austin, J., and Li, F.: On the relationship between the strength of the Brewer-Dobson circulation and the age of stratospheric air. Geophys. Res. Lett., 33, L17807, doi:10.1029/2006GL026867, 2006.

Austin, J., Wilson, J., Li, F., and Vomel, H.: Evolution of water vapor, and age of air in coupled chemistry-climate model simulations of the stratosphere, J. Atmos. Sci., 64 (3), 905-921, 2007.

Austin, J., et al.: The decline and recovery of total column ozone using a multi-model time series analysis, J. Geophys. Res., 115, D00M10, doi:10.1029/2010JD013857, 2010.

Brasseur, G., and Solomon, S.: Aeronomy of the Middle Atmosphere, 2nd edition, 452 pp., D. Reidel, Dordrecht, Holland, 1986.

Butchart, N., and Scaife, A.A.: Removal of chlorofluorocarbons by increased mass exchange between the stratosphere and the troposphere in a changing climate, Nature, 410, (6830), 799-802, 2001.

Butchart, N., et al.: Simulations of anthropogenic change in the strength of the Brewer-Dobson circulation, Climate Dyn., 27, 727-741, doi:10.1007/s00382-006-0162-4, 2006.

Butler, J.H, Battle, M., Bender, M.L., Montzka, S.A., Clarke, A.D., Saltzmank, E.S., Sucher, C.M., Severinghaus, J.P., and Elkins, J.W.: A record of atmospheric halocarbons during the twentieth century from polar firn air, Nature, 399, 749-755, 1999.

Chipperfield, M.P., and Feng, W.: Comment on: Stratospheric ozone depletion at northern mid latitudes in the 21st century: The importance of future concentrations of greenhouse gases nitrous oxide and methane, Geophys. Res. Lett., 30 (7), 1389, doi:10.1029/2002GL016353, 2003.

Chou, M-D, and Suarez, M.J.: A solar radiation parameterization for atmospheric studies, NASA Tech. Memo. NASA/TM-1999-104606, Vol. 15, 40 pp., 1999.

Chou, M-D, Suarez, M.J., Liang, X-Z, and Yan, M.-H.: A thermal infrared radiation parameterization for atmospheric studies, NASA Tech. Memo. NASA/TM-2001-104606, Vol. 19, 56 pp., 2001.

Considine, D.B, Douglass, A.R., and Jackman, C.H.: Effects of a polar stratospheric cloud parameterization on ozone depletion due to stratospheric aircraft in a two-dimensional model, J. Geophys. Res., 99, 18,879-18,894, 1994.

Considine, D.B., Rosenfield, J.E., and Fleming, E.L.: An interactive model study of the influence of the Mount Pinatubo aerosol on stratospheric methane and water trends, J. Geophys. Res., 106, D21, 27711-27727, 2001.

Crutzen, P.: Upper limits on atmospheric ozone reductions following increased application of fixed nitrogen to the soil, Geophys. Res. Lett., 3, 169-172, 1976.

Daniel, J.S., Fleming, E.L., Portmann, R.W., Velders, G.J.M., Jackman, C.H., and Ravishankara, A.R.: Options to accelerate ozone recovery: Ozone and climate benefits, Atmos. Chem. Phys., 10, 7697-7707, 2010.

Douglass, A.R., Stolarski, R.S., Schoeberl, M.R., Jackman, C.H., Gupta, M.L., Newman, P.A., Nielsen, J.E., and Fleming, E.L.: Relationship of loss, mean age of air and the distribution of CFCs to stratospheric circulation and implications for atmospheric lifetimes, J. Geophys. Res., 113, D14309, doi:10.1029/2007JD009575, 2008.

Duncan, B.N., Strahan, S.E., Yoshida, Y., Steenrod, S.D., and Livesey, N.: Model study of the cross-tropopause transport of biomass burning pollution, Atmos. Chem. Phys., 7, 3713-3736, 2007.

Engel, A., et al.: Age of stratospheric air unchanged within uncertainties over the past 30 years, Nature Geosci., 2, 28-31, 2009.

Eyring, V., et al.: Assessment of temperature, trace species, and ozone in chemistry-climate model simulations of the recent past, J. Geophys. Res., 111, D22308, doi:10.1029/2006JD007327, 2006.

Eyring, V., et al.: Multimodel projections of stratospheric ozone in the 21st century, J. Geophys. Res., 112, D16303, doi:10.1029/2006JD008332, 2007.

Eyring, V., et al.: Sensitivity of 21st century stratospheric ozone to greenhouse gas scenarios, Geophys. Res. Lett., 37, L16807, doi:10.1029/2010GL044443, 2010a.

Eyring, V., et al., Multi-model assessment of stratospheric ozone return dates and ozone recovery in CCMVal-2 models, Atmos. Chem. Phys., 10, 9451-9472, 2010b.

Fioletov, V. E., Bodeker, G. E., Miller, A. J., McPeters, R. D., and Stolarski, R.: Global ozone and zonal total ozone variations estimated from ground-based and satellite measurements: 1964-2000, J. Geophys. Res., 107(D22), 4647, doi:10.1029/2001JD001350, 2002.

Fisher, D.A., Hales, C.H., Filkin, D.L., Ko, M.K.W., Sze, N.D., Connell, P.S., Wuebbles, D.J., Isaksen, I.S.A., and Stordal, F.: Model calculations of the relative effects of CFCs and their replacements on stratospheric ozone, Nature, 344 (6266), 508-512, 1990.

Fleming, E.L., Jackman, C.H., Weisenstein, D.K., and Ko, M.K.W.: The impact of inter-annual variability on multi-decadal total ozone simulations, J. Geophys. Res., 112, D10310, doi:10.1029/2006JD007953, 2007.

Free, M., Seidel, D.J., Angell, J.K., Lanzante, J., Durre, I., and

Peterson, T.C.: Radiosonde Atmospheric Temperature Products for Assessing Climate (RATPAC): A new data set of large-area anomaly time series, J. Geophys. Res., 110, D22101, doi:10.1029/2005JD006169, 2005.

Garcia, R.R.: Parameterization of planetary wave breaking in the middle atmosphere, J. Atmos. Sci., 48 (11), 1405-1419, 1991.

Garcia, R.R., and Randel, W.J.: Acceleration of the Brewer-Dobson circulation due to increases in greenhous gases, J. Atmos. Sci., 65, 2731-2739, 2008.

Garcia, R.R., Marsh, D.R., Kinnison, D.E., Boville, B.A., and Sassi, F.: Simulation of secular trends in the middle atmosphere, 1950-2003, J. Geophys. Res., 112, D09301, doi:10.1029/2006JD007485, 2007.

Gelman, M. E., Miller, A.J., Jihnson, K.W., and Nagatani, R.N.: Detection of long term trends in global stratospheric temperature from NMC analyses derived from NOAA satellite data, Adv. Space Res., 6, 17-26, 1986.

Haigh, J.D., and Pyle, J.A.: A two-dimensional calculation including atmospheric carbon dioxide and stratospheric ozone, Nature, 279, 222-224, 1979.

Hall, T.M., and Waugh, D.W.: Influence of nonlocal chemistry on tracer distributions: Inferring the mean age of air from SF_6, J. Geophys. Res., 103, 13,327-13,336, 1998.

Hall, T.M., Waugh, D.W., Boering, K.A., and Plumb, R.A.: Evaluation of transport in stratospheric models, J. Geophys. Res., 104, 18,815-18,839, 1999.

Hansen, J., and Sato, M.: Greenhouse gas growth rates, Proc. Nat. Acad. Sci., 101, 46, 16109-16114, 2004.

Hansen, J., et al.: Climate simulations for 1880-2003 with GISS modelE, Climate Dyn., 29, 661-696, doi:10.1007/s00382-007-0255-8, 2007.

Herman, J.R., and Celarier, E.A.: Earth surface reflectivity climatology at 340-380 nm from TOMS data, J. Geophys. Res., 102 (D23), 28003-28011, 1997.

Intergovernmental Panel on Climate Change (IPCC): *Special Report on Emissions Scenarios*, edited by N. Nakicenovic et al., 599 pp., Cambridge Univ. Press, New York, 2000.

Intergovernmental Panel on Climate Change (IPCC): *Climate Change 2007: The Physical Science Basis. Contribution of Working Group I to the Fourth Assessment Report of the Intergovernmental Panel on Climate Change* [Solomon, S., D. Qin, M. Manning, Z. Chen, M. Marquis, K.B. Averyt, M. Tignor, H.L. Miller (eds.)]. Cambridge University Press, New York, 996 pp., 2007.

Jackman, C.H., Fleming, E.L., Chandra, S., Considine, D.B., and Rosenfield, J.E.: Past, present, and future modeled ozone trends with comparisons to observed trends, J. Geophys. Res., 101, 28,753-28,767, 1996.

Kaye, J. A., Penkett, S. A., and Ormond, F. M.: Report on concentrations, lifetimes, and trends of CFCs, halons, and related species, NASA Reference Publication 1339, 247 pp., 1994.

Kistler, R., et al.: The NCEP-NCAR 50-year reanalysis: Monthly means CD-ROM and documentation, Bull. Amer. Meteor. Soc., 82, 247-267, 2001.

Kodama, C., Iwasaki, T., Shibata, K., and Yukimoto, S.: Changes in the stratospheric mean meridional circulation due to increased CO_2: Radiation- and sea surface temperature-induced effects, J. Geophys. Res., 112, D16103, doi:10.1029/2006JD008219, 2007.

Lamarque, J.-F., et al.: Historical (1850-2000) gridded anthropogenic and biomass burning emissions of reactive gases and aerosols: methodology and application, Atmos. Chem. Phys., 10, 7017-7039, 2010.

Li, F., Austin, J., and Wilson, J.: The strength of the Brewer-Dobson circulation in a changing climate: coupled chemistry-climate model simulations, J. Climate, 21, 40-57, 2008.

Li, F., Stolarski, R.S., and Newman, P.A.: Stratospheric ozone in the post-CFC era, Atmos. Chem. Phys., 9, 2207-2213, 2009.

McPeters, R.D., Labow, G.J., and Logan, J.A.: Ozone climatological profiles for satellite retrieval algorithms, J. Geophys. Res., 112, D05308, doi:10.1029/2005JD006823, 2007.

Newchurch, M.J., Yang, E.-S., Cunnold, D.M., Reinsel, G.C., Zawodny, J.M., and Russell III, J.M.: Evidence for slowdown in stratospheric ozone loss: First stage of ozone recovery, J. Geophys. Res., 108, (D16), 4507, doi:10.1029/2003JD003471, 2003.

Newman, P.A., Schoeberl, M.R., Plumb, R.A., and Rosenfield, J.E.: Mixing rates calculated from potential vorticity, J. Geophys. Res., 93, 5221-5240, 1988.

Newman, P.A., et. al.: What would have happened to the ozone layer if chlorofluorocarbons (CFCs) had not been regulated?, Atmos. Chem. Phys., 9, 2113-2128, 2009.

Olsen, M.A., Schoeberl, M.R., and Nielsen, J.E.: Response of stratospheric circulation and stratosphere-troposphere exchange to changing sea surface temperatures, J. Geophys. Res., 112, D16104, doi:10.1029/2006JD008012, 2007.

Oman, L., Waugh, D.W., Pawson, S., Stolarski, R.S., and Newman, P.A.: On the influence of anthropogenic forcings on changes in the stratospheric mean age, J. Geophys. Res., 114, D03105, doi:10.1029/2008JD010378, 2009.

Park, J.H., Ko, M.K.W., Jackman, C.H., Plumb, R.A., Kaye, J.A., and Sage, K.H. (Editors): Models and Measurements Intercomparison II, NASA Tech. Memo., TM-1999-209554, 1999.

Pawson, S., Stolarski, R.S., Douglass, A.R., Newman, P.A., Nielsen, J.E., Frith, S.M., and Gupta, M.L.: Goddard Earth Observing System chemistry-climate model simulations of stratospheric ozone-temperature coupling between 1950 and 2005, J. Geophys. Res., 113, (D12103), doi:10.1029/2007JD009511, 2008.

Plumb, R.A., and Mahlman, J.D.: The zonally averaged transport characteristics of the GFDL general circulation/transport model, J. Atmos. Sci., 44, 298-327, 1987.

Portmann, R.W., and Solomon, S.: Indirect radiative forcing of the ozone layer during the 21st century, Geophys. Res. Lett., 34 L02813, doi:10.1029/2006GL028252, 2007.

Ramaswamy, V., et al.: Radiative forcing of climate change. In: *Climate Change 2001: The Scientific Basis. Contribution of Working Group I to the Third Assessment Report of the Intergovernmental Panel on Climate Change* [Houghton, J.T., et al. (eds.)]. Cambridge University Press, Cambridge, United Kingdom and New York, NY, USA, pp. 349-416, 2001a.

Ramaswamy, V., et al.: Stratospheric temperature trends: Observations and model simulations, Rev. Geophys., 39(1), 71-122, 2001b.

Randel, W.J., Wu, F., Gettelman, A., Russell III, J.M., Zawodny, J.M., and Oltmans, S.J.: Seasonal variation of water vapor in the lower stratosphere observed in Halogen Occultation Experiment data, J. Geophys. Res., 106, 14,313-14,325, 2001.

Randeniya, L.K., Vohralik, P.F., and Plumb, I.C.: Stratospheric ozone depletion at northern mid latitudes in the 21st century:

The importance of future concentrations of greenhouse gases nitrous oxide and methane, Geophys. Res. Lett., 29 (4), 1051, doi:10.1029/2001GL014295, 2002.

Ravishankara, A.R., Daniel, J.S., and Portmann, R.W.: Nitrous Oxide (N2O): the dominant ozone-depleting substance emitted in the 21st century. Science, 326, 123-125. 2009.

Ray, E.A., Moore, F.L., Elkins, J.W., Dutton, G.S., Fahey, D.W., Vomel, H., Oltmans, S.J., and Rosenlof, K.H.: Transport into the Northern Hemisphere lowermost stratosphere revealed by in situ tracer measurements, J. Geophys. Res., 104, 26,565-26,580, 1999.

Reinsel, G.C.: Trend analysis of upper stratospheric Umkehr ozone data for evidence of turnaround, Geophys. Res. Lett., 29 (10), 1451, doi:10.1029/2002GL014716, 2002.

Rontu Carlon, N., Papanastasiou, D.K., Fleming, E.L., Jackman, C.H., Newman, P.A., and Burkholder, J.B.: UV absorption cross sections of nitrous oxide (N_2O) and carbon tetrachloride ($CFCl_4$) between 210 and 350 K and the atmospheric implications, Atmos. Chem. Phys., 10, 6137-6149, 2010.

Rosenfield, J.E., Considine, D.B., Meade, P.E., Bacmeister, J.T., Jackman, C.H., and Schoeberl, M.R.: Stratospheric effects of Mount Pinatubo aerosol studied with a coupled two-dimensional model, J. Geophys. Res., 102, 3649-3670, 1997.

Rosenfield, J.E., and Douglass, A.R.: Doubled CO_2 effects on NO_y in a coupled 2D model, Geophys. Res. Lett., 25 (23), 4381-4384, 1998.

Rosenfield, J.E., A.R. Douglass, and D.B. Considine, The impact of increasing carbon dioxide on ozone recovery, J. Geophys. Res., 107, D6, doi:10.1029/2001JD000824, 2002.

Rosenfield, J.E., Frith, S.M., and Stolarski, R.S.: Version 8 SBUV ozone profile trends compared with trends from a zonally averaged chemical model, J. Geophys. Res., 110, D12302, doi:10.1029/2004JD005466, 2005.

Sander, S.P., et al.: Chemical kinetics and photochemical data for use in atmospheric studies, Evaluation number 15, *JPL Publ., 06-2*, 2006.

Shepherd, T.G., and Jonsson, A.I.: On the attribution of stratospheric ozone and temperature changes to changes in ozone-depleting substances and well-mixed greenhouse gases, Atmos. Chem. Phys., 8, 1435-1444, 2008.

Shine, K.P., et al.: A comparison of model-simulated trends in stratospheric temperatures, Quart. J. Roy. Meteor. Soc., 129, 1565-1588, 2003.

Solomon, S., Tuck, A.F., Mills, M., Heidt, L.E., and Pollock, W.H.: On the evaluation of ozone depletion potentials, J. Geophys. Res., 97, 825-842, 1992.

SPARC CCMVal, SPARC Report on the Evaluation of Chemistry-Climate Models, V. Eyring, T. G. Shepherd, D. W. Waugh (Eds.), SPARC Report No. 5, WCRP-132, WMO/TD-No. 1526, http://www.atmosp.physics.utoronto.ca/SPARC, 2010.

Stolarski, R.S., Douglass, A.R., Gupta, M., Newman, P.A., Pawson, S., Schoeberl, M.R., and Nielsen, J.E.: An ozone increase in the Antarctic summer stratosphere: A dynamical response to the ozone hole, Geophys. Res. Lett., 33, L21805, doi:10.1029/2006GL026820, 2006.

Stolarski, R.S., Douglass, A.R., Newman, P.A., Pawson, S., and Schoeberl, M.R.: Relative contribution of greenhouse gases and ozone-depleting substances to temperature trends in the stratosphere: A chemistry-climate model study, J. Climate, 23, 28-42, 2010.

Strahan, S.E., Duncan, B.N., and Hoor, P.: Observationally derived transport diagnostics for the lowermost stratosphere and their application to the GMI chemistry and transport model, Atmos. Chem. Phys., 7, 2435-2445, 2007.

Strobel, D.F.: Parameterization of the atmospheric heating rate from 15 to 120 km due to O_2 and O_3 absorption of solar radiation, J. Geophys. Res., 83, C12, 6225-6230, 1978.

Waugh, D.W., Oman, L., Kawa, S.R., Stolarski, R.S., Pawson, S., Douglass, A.R., Newman, P.A., and Nielsen, J.E.: Impacts of climate change on stratospheric ozone recovery, Geophys. Res. Lett., 36, L03805, doi:10.1029/2008GL036223, 2009.

World Meteorological Organization (WMO), Scientific Assessment of Ozone Depletion: 2002, Rep. 47 Global Ozone Research and Monitoring Project, Geneva, 2003.

World Meteorological Organization (WMO), Scientific Assessment of Ozone Depletion: 2006, Rep. 50 Global Ozone Research and Monitoring Project, Geneva, 2007.

World Meteorological Organization (WMO), Scientific Assessment of Ozone Depletion: 2010, Rep. 52 Global Ozone Research and Monitoring Project, Geneva, 2011.

Wuebbles, D.J.: Chlorocarbon emission scenarios: Potential impact on stratospheric ozone, Geophys. Res. Lett., 88 (C2), 1433-1443, 1983.